Semiclassical treatment of excitation and electron loss in $A^{q+}+H(1s)$ collisions using spherical Bessel functions

L. F. Errea,[1] L. Méndez,[1] B. Pons,[2] A. Riera,[1] I. Sevila,[1] and J. Suárez[1]
[1]*Laboratorio Asociado al CIEMAT de Física Atómica y Molecular en Plasmas de Fusión, Departamento de Química C-IX, Universidad Autónoma, 28049 Madrid, Spain*
[2]*Centre Lasers Intenses et Applications, UMR 5107 du CNRS, Université de Bordeaux–I, 351 Cours de la Libération, 33405 Talence, France*
(Received 7 March 2006; published 28 July 2006)

We perform monocentric close-coupling calculations to obtain partial and total cross sections for excitation and electron loss in bare $A^{q+}+H(1s)$ collisions, with $1 \leqslant q \leqslant 6$, for intermediate ($E=40$ keV/amu) to high ($E=7000$ keV/amu) impact energies. We use underlying basis sets of even-tempered Slater-type orbitals and confined spherical Bessel functions and compare the accuracy of the cross sections derived from these two implementations. Scaling rules are then established for the partial excitation cross sections of interest in fusion plasma research. We also undertake impact parameter first-Born calculations using the spherical Bessel underlying set to compare in the course of collision the close-coupling and perturbative descriptions of the ionization process.

DOI: 10.1103/PhysRevA.74.012722 PACS number(s): 34.10.+x, 34.50.Fa, 52.20.Hv

I. INTRODUCTION

The spectral emission, power balance, and ionization state of most astrophysical and laboratory fusion plasmas are commonly obtained by using the so-called generalized collisional-radiative model [1], which consists in solving the statistical balance equations relative to the equilibrium populations of the various species present in the plasma. In the fusion domain, ionic impurities with nuclear charges $q \leqslant 6$ are currently found in the plasmas of operating tokamak devices; the collisional rate coefficients and cross sections involving these ions and the fueling and/or diagnostic beam atoms (H,D) are key inputs to the balance equations, and their precision strongly influences the accuracy of the predictions derived from the collisional-radiative model.

During recent decades, a great number of theoretical and experimental works have thus been devoted to fill in the required collisional database. For example, the molecular close-coupling and perturbative continuum distorted wave (CDW) approaches to atomic collisions have been employed to calculate the state-selective capture cross sections for bare ion A^{q+} colliding on $H(1s)$, in the low and high impact energy ranges, respectively [2,3]. These data can be faithfully included in plasma modeling, and especially in analysis of charge-exchange spectroscopy (CXS) diagnostics [4], insomuch as the theoretical methods employed are certainly the most reliable ones in the respective energy ranges where they have been used. Ionization data for the same collisional systems and in similar energy regions can be found, e.g., in the works of Toshima [5] and Illescas and Riera [6], who employed the two-center atomic-orbital (2CAO) close-coupling formalism and, the classical trajectory Monte Carlo (CTMC) method with an improved hydrogenic initial distribution, respectively [7].

In this work, we complement these previous works dedicated to capture and ionization, and provide total and partial excitation cross sections for $A^{q+}+H(1s)$ collisions with $1 \leqslant q \leqslant 6$. We still shall be concerned with bare ions, in the intermediate to high $40 \leqslant E \leqslant 7000$ keV/amu energy region. To our knowledge and quite surprisingly, such a systematic study has never been undertaken up to now. This is mainly due to the restricted validity ranges of all the available theoretical methods. The application of perturbative approaches such as the eikonal impulse approximation (EIA) [8] is effectively restricted to the high impact energy range. On the contrary, the molecular close-coupling method is rather well suited to the low velocity regime. The addition of midcentered Gaussian pseudostates to the molecular basis allows us to extend the validity of the method to higher impact energies [9,10]; nevertheless, three-center molecular (3CMO) or atomic (3CAO) [11,12] calculations are not easy to perform because the underlying states are very prone to linear dependences. Many other theoretical schemes are formally well suited to provide accurate excitation cross sections. One of the most successful is certainly the 2CAO technique, the convergence of which has been thoroughly studied by Toshima [13] for the $p+H(1s)$ benchmark, following earlier works [14–16]. To represent in an optimal way the dynamical (two-center) properties of an ion-atom collision, the so-called basis generator method (BGM) prescribes to use a limited set of bound target eigenstates augmented with pseudostates constructed by recursive applications of the Schrödinger operator to the target states [17]. In practice, the hierarchy of pseudostates is built by using the (regularized) projectile interaction rather than the full Schrödinger operator [17]; this procedure has been successfully implemented for lowly charged ion-atom collisions (see, e.g., [18]), and some projectile bound eigenstates can be included in the calculations to improve the convergence of the expansion [19], as usual in the framework of close-coupling treatments. The lattice techniques [20–22], which are used to directly integrate the time-dependent Schrödinger equation (TDSE), are free from such a basis and other related contingencies, yet they remain quite cumbersome to be intensively employed, despite the recent advances in methodology and computer performances. Finally, the purely classical CTMC method

[23,24] is an appealing alternative, even though it cannot represent the interference patterns that appear at low impact energies [25,26] and it has some difficulties in reproducing, at high energies, the dipolar transitions that give rise to excitation at large impact parameters [27,28].

In this work, we employ a simple one-center atomic orbital (1CAO) close-coupling scheme, which consists in expanding the total electronic wave function in terms of eigenstates of the target. 1CAO calculations are obviously well suited to the high impact energy range where charge exchange is negligible. They are also pertinent in the intermediate energy regime, where all the inelastic processes are strongly coupled, provided the single-center basis is large enough to variationally represent charge exchange through transitions to target continuum states of high angular symmetry [29]. Such 1CAO expansions accordingly yield accurate cross sections for both target excitation and electron loss (capture+ionization), as shown, e.g., in [29,30]. However, various 1CAO implementations exist and mainly differ in the underlying basis used to construct the atomic eigenstates by diagonalization of the target Hamiltonian (see, e.g., [30,13]). It has been recently shown [31,32] that expansions in terms of exponentially decaying basis functions lead to unreliable descriptions of the ionization process in the asymptotic region. We further show in the present paper, using a representative large-scale basis of even-tempered Slater-type orbitals (STO), that these expansions also yield inaccurate cross sections for electron loss and excitation to high-lying bound states at low E. This failure is particularly patent for highly charged ion impact. We thus use an improved 1CAO expansion, in which spherical Bessel functions are employed to provide an accurate discretized representation of the atomic spectrum [31,32]. We obtain well-behaved excitation and electron-loss cross sections that adequately merge with the results derived from molecular calculations in the $E \leqslant 40$ keV/amu low-energy range [9,10,33]. We further explicitly check that our cross sections accurately tend to their first Born perturbative counterparts in the high-energy limit.

We then derive from our calculations semiempirical scaling rules for the partial excitation cross sections. They are slightly different from those established by Janev in [34], but also obey the asymptotic forms given by the advanced adiabatic theory [35] at low impact energy and by the classical impulse [36] and dipole close-coupling [37] approximations at high energy. The usefulness of such analytical scaling laws, which depend on the impact energy, projectile charge, and electron transition energy, is well known [38].

Finally, we show that the excellent agreement of the cross sections derived from our close-coupling and perturbative calculations in the high-energy region is not fortuitous. Further, both methods yield an identical description of the inelastic transition mechanisms through similar electronic densities and velocity fields. In particular, we prove that pertubative methods as simple as the first Born one confirm the classical [39] and close-coupling [27,31,40,41] quasifree expansion pictures of the ionization process. This is of great importance and strikingly reinforces the general characteristics of the wave function representing a dissociation event, as derived in [40].

The paper is organized as follows. We outline the monocentric close-coupling and first Born formalisms in Secs. II A and II B, respectively; we then present in Sec. II C the tools that we use to picture the ionization process, and we describe in Sec. II D the even-tempered STO and spherical Bessel expansions. Section III A presents our computed cross sections and the scaling fits are located in Sec. III B. The close-coupling and first Born descriptions of the ionization mechanism are displayed in Sec. III C and our conclusions are drawn in Sec. IV. Atomic units are used throughout unless explicitly stated.

II. IMPACT PARAMETER CLOSE-COUPLING AND PERTURBATIVE FRAMEWORKS

We employ the impact parameter method [38], in which the projectile follows rectilinear trajectories with constant velocity $\mathbf{v}$ and impact parameter $\mathbf{b}$, so that the internuclear vector is defined by $\mathbf{R}(t)=\mathbf{b}+\mathbf{v}t$. This is appropriate in the impact energy range considered ($E \geqslant 25$ keV/amu) insomuch as deviations from linear nuclear trajectories only appear at very low impact energies $E \leqslant 0.25$ keV/amu [42,43]. The electronic motion is described quantum mechanically. In the intermediate impact energy range, all the inelastic processes are strongly coupled and a variational close-coupling treatment is advisable. For higher impact energies, the collisional dynamics are mainly governed by weak direct transitions from the entry channel so that simpler pertubative treatments become adequate to an accurate theoretical description.

A. Monocentric close-coupling scheme

Monocentric close-coupling expansions for a single electron total wave function read

$$\Psi^{\mathrm{cc}}(\mathbf{r},v,b,t) = \sum_{E_n lm} a^{\mathrm{cc}}_{E_n lm}(v,b,t)\phi_{E_n lm}(\mathbf{r})e^{-iE_n t}, \qquad (1)$$

where $\phi_{E_n lm}(\mathbf{r})$ are atomic eigenstates mostly obtained by diagonalization of the target Hamiltonian H_0 in a basis of target-centered orbitals, and $E_n=\langle\phi_{E_n lm}|H_0|\phi_{E_n lm}\rangle$. The diagonalization procedure yields (L^2 square-integrable) wave functions of positive energy, usually called pseudostates, so that Ψ^{cc} spans both excitation ($E_n<0$) and ionization ($E_n>0$) channels. The amplitudes $a^{\mathrm{cc}}_{E_n lm}(v,b,t)$ are numerically obtained by solving the set of differential coupled equations that results from the substitution of the ansatz (1) in the eikonal equation,

$$\left(H_0 + V_A - i\left.\frac{\partial}{\partial t}\right|_{\mathbf{r}}\right)\Psi^{\mathrm{cc}}(\mathbf{r},v,b,t) = 0, \qquad (2)$$

where $V_A=-q/|\mathbf{r}-\mathbf{R}(t)|$ is the electron-projectile interaction. In this work, we have chosen to define the spherical states $\phi_{E_n lm}$ in the rotating molecular reference frame, with the quantization axis along the $\hat{\mathbf{R}}$ direction; the V_A potential matrix elements $\langle\phi_{E_n lm}|V_A|\phi_{E_{n'} l'm'}\rangle$ thus obey a $\delta_{mm'}$ selection rule and their multipole expansions are simplified. We further make use of reflection symmetry with respect to the $(\mathbf{v},\mathbf{b})$ collision plane to define real atomic wave functions with $m \geqslant 0$ and an angular part given by

$$\mathcal{Y}_l^{m=0}(\theta,\phi) = Y_l^{m=0}(\theta,\phi),$$

$$\mathcal{Y}_l^{m\neq 0}(\theta,\phi) = \frac{1}{\sqrt{2}}[Y_l^m(\theta,\phi) + (-1)^m Y_l^{-m}(\theta,\phi)]. \quad (3)$$

Under the geometrical transformation from the laboratory-fixed reference frame to the molecular one, the dynamical operator in Eq. (2) splits into radial and rotational couplings [38]: $\partial/\partial t|_{\mathbf{r}} = (vt^2/R)\partial/\partial R + (bv/R^2)iL_y$. Since $\langle \phi_{E_n lm}|\partial/\partial R|\phi_{E_{n'}l'm'}\rangle = 0$ and $\langle \phi_{E_n lm}|iL_y|\phi_{E_{n'}l'm'}\rangle = \mp \delta_{E_n E_{n'}}\delta_{ll'}\delta_{m\pm 1 m'} C\sqrt{l(l+1)-m(m\pm 1)}/2$, where $C=\sqrt{2}$ if m or $m'=0$ and $C=1$ otherwise, we finally obtain the differential equations,

$$\frac{da^{\mathrm{cc}}_{E_n lm}(v,b,t)}{dt} = i\sum_{E_{n'}l'} a^{\mathrm{cc}}_{E_{n'}l'm}(v,b,t) \times \left\langle \phi_{E_n lm}\left|\frac{q}{|\mathbf{r}-\mathbf{R}(t)|}\right|\phi_{E_{n'}l'm}\right\rangle \times e^{-i(E_{n'}-E_n)t} \pm \frac{bv}{R^2}\frac{C}{2}\sqrt{l(l+1)-m(m\pm 1)} \times a^{\mathrm{cc}}_{E_n lm\pm 1}(v,b,t). \quad (4)$$

This coupled equation set is integrated from $t_{\mathrm{in}}=-400/v$ a.u., where $a^{\mathrm{cc}}_{E_n lm}(v,b,t_{\mathrm{in}}) = \delta_{E_n lm,-0.5\ 0\ 0}$ for the H($1s$) initial state, up to $t_{\max}=400/v$ a.u. large enough in order that all amplitudes of interest have reached their asymptotic values. The transition probabilities, which are trivially obtained as $P^{\mathrm{cc}}_{E_n lm}(v,b,t) = |a^{\mathrm{cc}}_{E_n lm}(v,b,t)|^2$, can be displayed for a given nuclear trajectory as functions of the time t to yield the so-called "collision history." The cross sections are obtained by integrating, at the end of the collision, the weighted probabilities over the impact parameter,

$$\sigma^{\mathrm{cc}}_{E_n lm}(v) = 2\pi \int b P^{\mathrm{cc}}_{E_n lm}(v,b,t_{\max}) db. \quad (5)$$

We identify the sum of all pseudostate populations to the ionization probability. Such a definition does not provide a separation of the capture and ionization fluxes. Indeed, the energy of a captured electron with respect to the target asymptotically reduces to its kinetic term, which is definite positive. The capture flux can thus be formally described in terms of continuum target states. According to this, and because of the variational character of the monocentric close-coupling method, we shall assist to an accumulation of the capture flux onto the pseudostates of our expansion, which does not include any explicit representation of capture channels. So what we refer to as ionization shall rather coincide, in the impact energy range where capture is not negligible ($E \lesssim 100$ keV/amu), with the so-called electron loss (i.e., capture+genuine ionization) flux. The capture and ionization contributions to electron loss cannot be unambiguously separated since we use in practice finite sets of target orbitals whose overlaps with projectile eigenstates vanish in the limit $R\to\infty$. Furthermore, we will show in the following section that the implicit account for capture can result in an *unphysical* contamination of highly excited bound states when the underlying basis used to diagonalize H_0 is not flexible enough to provide an accurate description of the target continuum. It must be noted that the reverse situation appears in standard molecular treatments, without pseudostates, where the ionizing flux is implicitly represented and trapped by the bound states in the first stages of the collision [44–47].

B. Impact parameter first Born approximation

The inelastic transitions are weaker as the impact energy increases, and the perturbative approximations, which are easier to implement than variational methods, become appropriate when $q/v<1$. As a part of the impact velocity region considered in this work complies with this criterion, we also perform semiclassical first Born ($B1$) calculations to obtain excitation and ionization cross sections for $40 \leqslant E \leqslant 10\,000$ keV/amu.

We still employ the impact parameter approach, whose validity domain largely encompasses the $B1$ one. The transition amplitudes $a^{B1}_{E_n lm}(v,b,t)$, which build the perturbative total wave function

$$\Psi^{B1}(\mathbf{r},v,b,t) = \Phi_{-0.5\ 0\ 0}(\mathbf{r})e^{it/2} + \sum_{E_n lm, E_n\neq -0.5} a^{B1}_{E_n lm}(v,b,t) \times \Phi_{E_n lm}(\mathbf{r})e^{-iE_n t}, \quad (6)$$

read

$$a^{B1}_{E_n lm}(v,b,t) = \lim_{t_{\max}\to\infty} -i\int_{-t_{\max}}^{t} \langle \Phi_{E_n lm}|V_A|\Phi_{-0.5\ 0\ 0}\rangle \times e^{-i(-0.5-E_n)t'}dt', \quad (7)$$

where the $\Phi_{E_n lm}$ atomic states are defined in the laboratory-fixed reference frame,

$$|\Phi_{E_n lm}\rangle = \sum_{m'} \mathcal{R}^l_{m,m'}(\theta)|\phi_{E_n lm'}\rangle \quad (8)$$

with $\theta=\arccos(vt/R)$ and $\mathcal{R}^l_{m,m'}$ is the rotation matrix associated to the real harmonics (3). Since we calculate the V_A matrix elements in the rotating reference frame, we use Eq. (8) and the $\delta_{mm'}$ selection rule for $\langle \phi_{E_n lm}|V_A|\phi_{E_{n'}l'm'}\rangle$ to obtain

$$a^{B1}_{E_n lm}(v,b,Z=vt) = \lim_{Z_{\max}\to\infty} -\frac{iq}{v}\int_{-Z_{\max}}^{Z} \mathcal{R}^l_{m,0}(\theta) \times \left\langle \phi_{E_n l0}\left|\frac{1}{|\mathbf{r}-\mathbf{R}(t)|}\right|\phi_{-0.5\ 0\ 0}\right\rangle \times e^{i(0.5+E_n)Z'/v}dZ' \quad (9)$$

with $Z_{\max}=vt_{\max}$.It is worth noting that the $\mathcal{R}^l_{m,0}$ matrix is related to the usual rotation one $r^l_{m,0}$, as defined in [48], through $\mathcal{R}^l_{0,0}=r^l_{0,0}$ and $\mathcal{R}^l_{m,0}=\sqrt{2}r^l_{m,0}$ for $m\neq 0$.

It can be seen from Eq. (9) that the impact parameter $B1$ transition probabilities $P^{B1}_{E_n lm}(v,b,Z) = |a^{B1}_{E_n lm}(v,b,Z)|^2$ and corresponding cross sections $\sigma^{B1}_{E_n lm}(v) = 2\pi\int b P^{B1}_{E_n lm}(v,b,Z_{\max})db$ quadratically depend on q. This is

of great convenience insomuch as the $B1$ results for a given $A^{q+}+\mathrm{H}(1s)$ system are thus immediately deduced from the ones relative to $\mathrm{H}^{+}+\mathrm{H}(1s)$ without the need for further computation; one just has to apply the q^2 scaling rule.

C. Imaging the ionization process

To the best of our knowledge, the reliability and limitations of perturbative descriptions of the ionization process have only been shown in the asympotic collisional region by means of the comparison of computed differential and total cross sections with experimental data (see, for instance, [49]). In this work, we check whether the close-coupling and $B1$ approaches yield similar pictures of the ionization process *throughout the collision*.

Consistently with the definition of the ionization probabilities and cross sections, we obtain the ionizing parts $\Psi_{\mathrm{ion}}^{\mathrm{cc},B1}(\mathbf{r},v,b,t)$ of the total close-coupling (cc) and perturbative ($B1$) total wave functions from the respective Eqs. (1) and (6) under the restriction $E_n>0$. We thus compute the momentum counterparts $\Psi_{\mathrm{ion}}^{\mathrm{cc},B1}(\mathbf{p},v,b,t)$ using (fast) Fourier transform. Time samplings of both configuration and momentum ionizing densities $\rho_{\mathrm{ion}}^{\mathrm{cc},B1}=|\Psi_{\mathrm{ion}}^{\mathrm{cc},B1}|^2$ can then be displayed along a selected (v,b) nuclear trajectory, as functions of scaled time $Z=vt$. More illustrative pictures can be obtained by calculating the electronic average velocity field,

$$\mathbf{v}_{\mathbf{e}}^{\mathrm{cc},B1}(\mathbf{r},v,b,t)=\mathbf{J}_{\mathrm{ion}}^{\mathrm{cc},B1}(\mathbf{r},v,b,t)/\rho_{\mathrm{ion}}^{\mathrm{cc},B1}(\mathbf{r},v,b,t), \quad (10)$$

where $\mathbf{J}_{\mathrm{ion}}^{\mathrm{cc},B1}$ is the current density,

$$\mathbf{J}_{\mathrm{ion}}^{\mathrm{cc},B1}(\mathbf{r},t)=\frac{i}{2}[\Psi_{\mathrm{ion}}^{\mathrm{cc},B1^*}(\mathbf{r},t)\,\nabla\,\Psi_{\mathrm{ion}}^{\mathrm{cc},B1}(\mathbf{r},t) - \Psi_{\mathrm{ion}}^{\mathrm{cc},B1}(\mathbf{r},t)\,\nabla\,\Psi_{\mathrm{ion}}^{\mathrm{cc},B1^*}(\mathbf{r},t)], \quad (11)$$

to finally display arrow diagrams $\{\mathbf{r},\mathbf{v}_{\mathbf{e}}\}$ in which the correspondence between electron position and average velocity is established at any time t.

D. Basis sets

As mentioned in the Introduction, various implementations of the monocentric close-coupling method exist; they mainly differ in the underlying basis sets used to construct the target eigenstates through diagonalization of H_0. In this work, we employed two large-scale bases. The first one consists of even-tempered STOs to obtain the radial part of $\phi_{E_n lm}(\mathbf{r})$ as

$$\phi_{E_n l}(r)=\sum_j c_j^{E_n l} r^l e^{-\alpha_j r}. \quad (12)$$

The parameters α_j are in geometrical series, which can be different for each l symmetry: $\alpha_j=\alpha_0\beta^j$ with $0\leqslant j\leqslant j_{\max}$. The STO basis is thus characterized by the maximum angular momentum $l_{\max}$ and the geometrical series $\{\alpha_0,\beta,j_{\max}\}_{l=0,\ldots,l_{\max}}$. In the present calculations, we use $l_{\max}=8$ and set $\{\alpha_0=0.001,\ \beta=1.3,\ j_{\max}=40\}$ for all l. Such a large $l_{\max}$ value is necessary to reach convergence (within less than 10%) for both excitation and electron-loss cross sections at the lowest impact energy considered ($E=40$ keV/amu). We thus have a quite huge set of 369 orbitals, which gives rise to 1845 real eigenstates with $0\leqslant m\leqslant l$. Among them, the description of the 120 bound states with $1\leqslant n\leqslant 8$ can be regarded as exact. The diagonalization further yields 837 bound states that are combinations of Rydberg states with $n\geqslant 9$; an accurate description of individual Rydberg states would necessitate the use of an almost infinite basis with $\alpha_0\to 0$, $\beta\to 1$, and $j_{\max}\to\infty$ that spans the entire configuration space. Such an infinite set would obviously also lead to an exact representation of continuum states; in practice, the truncation of the basis results in 888 pseudostates, with $E_n>0$, that are exponentially spaced in energy scale [32]. These pseudostates closely represent the inner part of the exact continuum states but rapidly vanish for $r>15$ a.u. because of the exponentially decaying r behavior of the basis functions [32]. In this respect, it is important to note that our STO set is large enough to be considered as representative of all alternative expansions in terms of exponentially decaying basis functions such as Gaussian [5], scaled hydrogenic [50] and Sturmian [51] orbitals.

We also employ an improved 1CAO approach in terms of spherical Bessel functions confined in a hermetic spherical box of radius $r_{\max}$ centered on the target [31,32]. As the electron motion is confined within the spherical box, all wave functions vanish beyond $r_{\max}$ so that the atomic spectrum reduces to an infinite *but discrete* set of stationary modes. For a given (l,m) angular symmetry, the pseudocontinuum modes are equally spaced by $\Delta p\sim\pi/r_{\max}$ in momentum space, yielding a state density $d(E)=r_{\max}/\pi\sqrt{2E}$ on the energy scale. Within the box, the radial part of the eigenfunctions is obtained by diagonalizing H_0 in the basis of all the spherical Bessel functions $j_l(kr)$, with $0\leqslant k\leqslant k_{\max}$ and $0\leqslant l\leqslant l_{\max}$, which fulfill the continuity condition $j_l(kr_{\max})=0$. In this work, we employ $l_{\max}=8$, as for the STO basis, and use $r_{\max}=100$ a.u. and $k_{\max}=2.5$ a.u. Higher values of k would be necessary to reproduce the strongly peaked behavior of the lowest-lying eigenstates about the H^{+} nucleus; as electron emission with momentum $p>2.5$ a.u. is negligible, we avoid cumbersome calculations by adding explicitly the $\mathrm{H}(1s)$ and $\mathrm{H}(2p)$ eigenstates to the basis before diagonalizing H_0. We include real spherical harmonics up to $m=5$ insomuch as the final populations of states with $m\geqslant 6$ can be depreciated, so that our basis totals up to 3034 states. The description of the 56 lowest bound states with $1\leqslant n\leqslant 6$ can be regarded as exact. Since $\phi_{E_n lm}(r\geqslant r_{\max})=0$, the diagonalization procedure yields only 105 further bound states that overlap the inner part of true Rydberg states. Such a discretized representation of Rydberg series already ensures the convergence of the collisional results associated to lower ($n\leqslant 6$) and higher (continuum) states [52]. The remaining 2873 diagonalized states are pseudocontinuum modes whose energies extend up to $E_n\sim k_{\max}^2/2$. These pseudocontinuum states perfectly fit the exact ones within the box [32], and one can verify the completeness of the underlying Bessel basis with respect to the description of all the modes, by comparing the density of pseudocontinuum states obtained after diagonalization of H_0 with the expected one, $d=r_{\max}/\pi\sqrt{2E}$ [32].

We have shown that a very accurate representation of the continuum is required for a reliable description of the

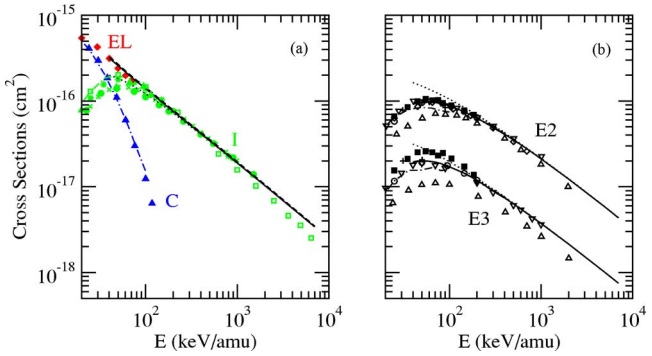

FIG. 1. (Color online) Total ionization (I), capture (C), and electron-loss (EL) (a) and $n=2$ ($E2$) and 3 ($E3$) excitation (b) cross sections in $H^+ + H(1s)$ collisions, as functions of the impact energy E. Theoretical results: Present close-coupling Bessel (—), first Born (……), and STO (---) calculations;—-—, 3CMO cross sections [9]; □, hydrogenic CTMC ionization cross section [6]; ∗, 2CAO ionization cross section [13]; ×, CDW-EIS ionization cross section [57]; △, microcanonical CTMC excitation cross sections [60]; +, 1CAO excitation cross sections [30]; ◇ and ▽, TDSE excitation cross sections of [21,20], respectively; ○, EIA excitation cross sections [8]. Experimental data for capture (▲) [58], ionization (●) [53–55] (▲) [56], and excitation (■) [59]. Capture [58] and ionization [53–55] cross sections have been added to yield the experimental electron-loss cross section (◆).

ionization process [31,32]. Accordingly, we have used the underlying Bessel basis in our $B1$ calculations, since the STO expansion inevitably leads to unphysical ionizing distributions in the outgoing part of the collision, as soon as the cloud expands beyond the limited $r \lesssim 15$ a.u. range. Nonetheless, we explicitly showed, in the case of $\bar{p}+H(1s)$ collisions [31,32], that most of the inelastic transitions from the entry channel occur within this limited range; the excitation and ionization STO cross sections were thus found to be as accurate as the Bessel ones. In the following section, we shall check that this property holds for positively (and highly) charged ions.

III. RESULTS

A. Close-coupling and perturbative cross sections for $A^{q+}+H(1s)$ collisions

1. $p+H(1s)$ collisions

In Fig. 1(a), we display as a function of the impact energy E the electron-loss cross sections obtained by means of our 1CAO and $B1$ calculations for $p+H(1s)$ collisions. As for $\bar{p}+H(1s)$, the STO and Bessel 1CAO approaches yield almost identical cross sections over the whole impact energy range. Our results are compared with the experimental data of Shah *et al.* [53–55] and Kerby *et al.* [56] for ionization, and with the ionization cross sections derived from hydrogenic CTMC [6], 2CAO [13], CDW-EIS [57], and 3CMO [9] calculations. We also report the experimental electron-loss cross section obtained by adding the data of McClure [58] and Shah *et al.* [53–55] for capture and ionization, respectively, to emphasize how our 1CAO calculations fairly reproduce the whole electron-loss flux in the intermediate energy region where capture cannot be neglected with respect to ionization.

For $E > 100$ keV, the B1 cross section is in close agreement with the close-coupling and CDW-EIS ones, and all of them nicely merge with the experimental data. The $B1$ approximation fails in reproducing the variational 1CAO results at lower energies; higher-order perturbative treatments would improve the comparison with the close-coupling results.

The CDW-EIS method provides an ionization cross section in excellent agreement with the measurements of Shah *et al.* over the entire impact energy range. This is at variance with the 2CAO, 3CMO, and CTMC predictions that lie ~20% above the same experimental results up to $E=100$ keV. The agreement of these latter calculations with the measurements of Kerby *et al.* is slightly better for $E \geqslant 67$ keV, but a discrepancy comparable to the previous one still appears near the maximum of the cross section. If the validity of the normalization procedure employed by Shah *et al.*, based on 1000–1500 keV Born values, can be questioned [13], this is not the case for the data of Kerby *et al.*, who designed apparatus and procedures for direct measurement of absolute cross sections. However, the striking agreement of all close-coupling and classical calculations cannot be coincidental and encourages further experimental investigations.

In Fig. 1(b), we present our computed cross sections for excitation into the $n=2$ and 3 shells in $p+H(1s)$ collisions. Our 1CAO and $B1$ results are compared with the experimental cross sections of Park *et al.* [59], with the 3CMO results of Errea *et al.* [9], with the results of Schultz *et al.* [20] and Tong *et al.* [21] who employed lattice techniques to solve TDSE, with the prior EIA results of Rodríguez and Miraglia [8], with the 1CAO STO results of Martín [30], and with the CTMC results of Reinhold *et al.* [60].

As before, the STO and Bessel underlying bases lead to similar 1CAO cross sections from $E=40$ keV up to the highest impact energies. The results of Martín, who has used $l_{max}=5$ in his STO calculations, are almost identical to ours; in practice, our higher value of l_{max} is necessary for higher projectile charges, which induce stronger polarization effects on the electronic cloud. The $B1$ approximation becomes accurate for $E \geqslant 200$ keV, whereas EIA effectively provides reliable results down to $E/q=25$ keV/amu, as assumed in [8].

The microcanonical CTMC calculations of Reinhold *et al.* underestimate the excitation cross sections from low to high impact energies. As the excitation processes mainly occur through long-range ($b \gg a_0$) transitions that involve the outer part of the target-centered electronic cloud, we safely trace back the origin of the underestimation to the use of the too compact microcanonical distribution with $E_n=-0.5$ a.u. We have demonstrated this effect in [10,25] for capture and ionization at small v, by considering sophisticated classical initial conditions that improve the cross sections; similar investigations remain to be performed in the case of excitation to verify our assumption.

The agreement of all the semiclassical cross sections is remarkable, with the exception of the triple-center molecular results for $E \geqslant 40$ keV; as previously noted, the 3CMO

TABLE I. Cross sections (10^{-17} cm^{-2}) for excitation into $2l$, $3l$, and more excited $n \geqslant 4$ (Rest) levels, and for electron-loss (EL) in $H^+ + H(1s)$ collisions, as functions of the impact energy E. For $E \geqslant 75$ keV/amu, capture can be neglected with respect to ionization [see Fig. 1(a)] so that $\sigma_{EL} \sim \sigma_{ion}$.

E (keV/amu)	$n=2$	$2s$	$2p$	$n=3$	$3s$	$3p$	$3d$	Rest	EL
40	9.3681	1.9266	7.4415	1.9543	0.4361	1.1621	0.3561	1.7590	31.701
50	9.6967	1.7468	7.9499	2.0028	0.3958	1.2934	0.3136	1.7860	25.865
75	9.3649	1.3162	8.0487	1.8947	0.2923	1.3585	0.2439	1.6642	17.978
100	8.7614	1.0249	7.7365	1.7071	0.2233	1.2981	0.1857	1.4764	13.892
150	7.3370	0.6924	6.6446	1.4072	0.1468	1.1447	0.1157	1.1954	9.7074
200	6.3074	0.5170	5.7904	1.1852	0.1077	0.9922	0.0852	0.9977	7.5729
400	4.1049	0.2517	3.8532	0.7432	0.0509	0.6528	0.0395	0.6157	4.1706
600	3.0982	0.1653	2.9329	0.5512	0.0331	0.4924	0.0257	0.4543	2.9419
800	2.5137	0.1233	2.3904	0.4441	0.0246	0.4004	0.0191	0.3651	2.3004
1000	2.1171	0.0978	2.0192	0.3735	0.0195	0.3389	0.0151	0.3055	1.8918
2000	1.2313	0.0484	1.1829	0.2147	0.0096	0.1976	0.0075	0.1749	1.0342
5000	0.5805	0.0192	0.5613	0.1001	0.0038	0.0934	0.0030	0.0811	0.4598
7000	0.4336	0.0137	0.4199	0.0750	0.0027	0.0702	0.0021	0.0607	0.3405

formalism is not the more adequate in this impact energy region, and we verify in Fig. 1(a), for electron-loss, and in Fig. 1(b), for excitation, that 1CAO approaches yield a well-suited continuation of the molecular results to $E > 40$ keV. The agreement between the semiclassical results and the measurements of Park *et al.* is much better for $n=2$ than for $n=3$: the $n=3$ experimental data lie $\sim$20% above the corresponding theoretical cross sections for $E \leqslant 100$ keV. Park *et al.* have extracted absolute cross sections through a normalization of the $n=2$ energy-loss spectrum to the corresponding $B1$ cross section at $E=200$ keV. In practice, they used the $B1$ value obtained by Bates and Griffing [61], 6.637×10^{-17} cm^2. Our impact-parameter $B1$ value for the same $n=2$ cross section is 6.86×10^{-17} cm^2 and differs from the previous value by only 3.2%. We also performed purely quantum (analytical) $B1$ calculations and have obtained 6.84×10^{-17} cm^2, a value that is fully compatible with our impact parameter calculations and with the value obtained by Mandal *et al.* [62], 6.85×10^{-17} cm^2. Even the renormalization of the measurements with our more accurate 1CAO Bessel $n=2$ cross section, i.e., 6.31×10^{-17} cm^2, would not substantially modify the experimental data. We thus conclude that the theoretical/experimental discrepancy on the $n=3$ cross section around its maximum is not due to the normalization procedure; its origin remains an open question.

Table I contains the excitation and electron-loss cross sections obtained by means of the 1CAO Bessel approach for $40 \leqslant E \leqslant 7000$ keV/amu. Table I details the partial $H(2l)$ and $H(3l)$ excitation cross sections, and includes the sum of the cross sections for excitation into higher $n \geqslant 4$ levels. For $E \geqslant 100$ keV, the contribution of capture to the target electron loss can be neglected [see Fig. 1(a)] so that the electron-loss cross section can be taken as the genuine ionization one; this threshold is marked in Table I.

2. $He^{2+} + H(1s)$ *collisions*

Our computed electron-loss cross sections for $He^{2+} + H(1s)$ collisions are displayed in Fig. 2(a) as functions of E. The Bessel 1CAO results perfectly merge with the 3CMO cross section of Errea *et al.* [9] around $E=40$ keV/amu, where capture is the dominant process. The agreement with the experimental data obtained by adding the cross sections of Shah *et al.* for capture [64] and ionization [53,63] is also very satisfactory for $E \leqslant 60$ keV/amu. In the $60 < E \leqslant 200$ keV/amu energy range, the 2CAO [5], 3CMO [9], hydrogenic CTMC [6] and present 1CAO calculations provide ionization, and therefore electron-loss cross sections lying $\sim$20% above the measurements. In this respect, it is worth noting that the (not absolute) experimental cross section for ionization has been deduced by reference to proton impact for which a comparable scaling factor comes out be-

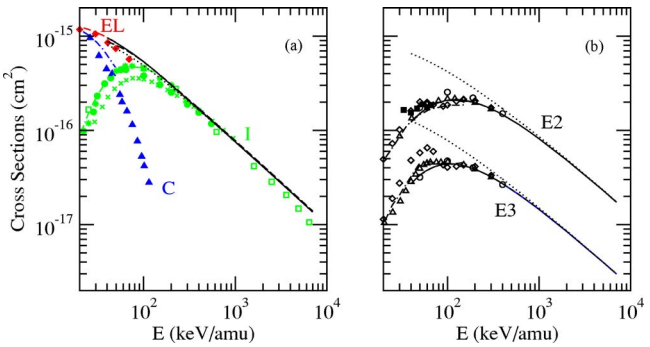

FIG. 2. (Color online) Total ionization (I), capture (C), and electron-loss (EL) (a) and $n=2$ ($E2$) and 3 ($E3$) excitation (b) cross sections in $He^{2+} + H(1s)$ collisions, as functions of the impact energy E. Theoretical results: Present close-coupling Bessel (—), first Born (……), and STO (---) calculations;———, 3CMO cross sections [9]; □, hydrogenic CTMC ionization cross section [6]; ∗, 2CAO ionization cross section [5]; ×, CDW-EIS ionization cross section [57]; ◇ and △, 2CAO excitation cross sections of [67,16], respectively; ○, EIA excitation cross sections [8]. Experimental data for capture [64] (▲), ionization [53,63] (●), and excitation (■) [66]. Capture [64] and ionization [53,63] cross sections have been added to yield the experimental electron-loss cross section (♦).

TABLE II. Cross sections (10^{-17} cm^2) for excitation into $2l$, $3l$, and more excited $n \geqslant 4$ (Rest) levels, and for electron-loss (EL) in $He^{2+}+H(1s)$ collisions, as functions of the impact energy E. For $E \geqslant 150$ keV/amu, $\sigma_{EL} \sim \sigma_{ion}$ [see Fig. 2(a)].

E (keV/amu)	$n=2$	$2s$	$2p$	$n=3$	$3s$	$3p$	$3d$	Rest	EL
40	12.155	3.0736	9.0818	2.7020	0.5814	1.3420	0.7786	2.5550	96.146
50	15.031	3.2478	11.783	3.3399	0.6512	1.7748	0.9139	3.1411	85.067
75	18.963	3.1520	15.811	4.1848	0.6711	2.5572	0.9565	3.8714	66.012
100	20.879	2.8409	18.038	4.3946	0.6088	2.9104	0.8754	3.9839	53.469
150	20.877	2.2508	18.626	4.2186	0.4800	3.1328	0.6059	3.7052	38.585
200	19.643	1.8187	17.824	3.8545	0.3827	3.0158	0.4559	3.3323	30.359
400	14.674	0.9804	13.693	2.7129	0.2002	2.3149	0.1977	2.2774	16.725
600	11.564	0.6586	10.906	2.0848	0.1329	1.8311	0.1208	1.7322	11.771
800	9.5729	0.4947	9.0782	1.7074	0.0993	1.5217	0.0864	1.4111	9.1947
1000	8.1574	0.3937	7.7637	1.4497	0.0788	1.3044	0.0666	1.1901	7.5573
2000	4.8459	0.1950	4.6509	0.8475	0.0388	0.7775	0.0312	0.6912	4.1301
5000	2.3095	0.0772	2.2323	0.3988	0.0153	0.3714	0.0121	0.3229	1.8373
7000	1.7280	0.0551	1.6729	0.2992	0.0109	0.2797	0.0086	0.2422	1.3610

tween the data of Shah *et al.* [53–55] and the most accurate theoretical values.

The $B1$ approximation is valid for $E \gtrsim 300$ keV/amu, in accordance with the perturbative criterion $q/v < 1$. The higher-order CDW-EIS approach [57] allows to reproduce the maximum of the ionization cross section around 80 keV/amu, but leads to a significant underestimation of the cross section in the low- and intermediate-energy ranges.

As for $p+H(1s)$, the hydrogenic CTMC ionization cross section is lower than our semi-classical one for $E \gtrsim 500$ keV/amu; nonetheless, it exhibits an $\sim \ln(E)/E$ energy behavior. The comparison of classical and semiclassical weighted probabilities $bP(b)$ shows that CTMC is not able to reproduce the long-range dipolar transitions, which are important at high E, and that this lack of large-b transitions is partly compensated by an overestimation of the ionization probabilities from small to intermediate b [27]. The $\sim \ln(E)/E$ behavior of the cross section is classically recovered insomuch as most of the intermediate-range ($2 \leqslant b \leqslant 6$) transitions are also of dipolar type, yielding a $p\pi$-shaped classical ionizing density [65].

We present in Fig. 2(b) our $n=2$ and 3 excitation cross sections and compare them with the experimental data of Hughes *et al.* [66], the 2CAO results of Fritsch *et al.* [67] and Kuang and Lin [16], the 3CMO cross sections of Errea *et al.* [9], and the pertubative EIA results of Rodriguez and Miraglia [8].

No significant differences appear between the STO and Bessel cross sections over the whole impact energy range. The $B1$ approximation provides accurate excitation cross sections for $E \gtrsim 1000$ keV/amu; this lower bound is higher than the one found for $p+H(1s)$ collisions, as expected from the fact that the $B1$ low-energy validity limit is proportional to q.

Our $n=2$ 1CAO and 3CMO cross sections adequately coalesce at $E=40$ keV/amu. For higher impact energies, 3CMO leads to an underestimation of the cross section and our present results better agree with the 2CAO result of Kuang and Lin, and to a lesser extent with the EIA perturbative cross section. The agreement of our semiclassical cross section with the experimental data of Hughes *et al.* is satisfactory.

With respect to the $n=3$ excitation cross section, one can appreciate in Fig. 2(b) the extreme sensitivity of the 2CAO results to the number and location of pseudostates included in 2CAO calculations by comparing the results of Fritsch *et al.* and those of Kuang and Lin. The former authors introduced on both nuclear centers a few pseudostates with nuclear charge $q=3$ in order to improve the description of the molecular effects that control the collisional mechanisms at low impact velocities. Kuang and Lin augmented their two-center atomic bound state basis only with target-centered pseudostates. The latter (and larger) atomic basis leads to a better agreement of atomic and molecular $n=3$ excitation cross sections [see Fig. 2(b)]. Our 1CAO calculations tend to reproduce the 2CAO and 3CMO $n=3$ cross sections at low impact energies. Nevertheless, the 1CAO cross sections do not present a flat shape around $E=70$ keV/amu, unlike the 2CAO and 3CMO results. One could invoke a bad description of decisive two-center effects by our 1CAO basis with limited l_{max}. We thus have studied the convergence of our 1CAO $n=3$ cross sections with respect to increasing l_{max} and found that they are converged within 5% for $E \gtrsim 50$ keV/amu. We therefore trust in the reliability of our 1CAO results and stress that further convergence checks should have to be performed in the 2CAO and 3CMO cases.

Our 1CAO Bessel cross sections for electron-loss and excitation to nl levels with $n=2,3$ are given in Table II; the table also includes the sum of excitation cross sections to higher ($n \geqslant 4$) channels.

3. $Li^{3+}+H(1s)$ *collisions*

In Fig. 3(a), we display as functions of the impact energy E the electron-loss cross sections obtained by means of our 1CAO calculations for $Li^{3+}+H(1s)$ collisions. They agree

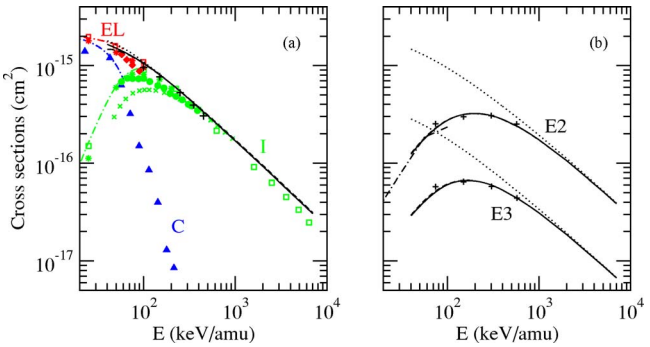

FIG. 3. (Color online) Total ionization (I), capture (C), and electron-loss (EL) (a) and $n=2$ ($E2$) and 3 ($E3$) excitation (b) cross sections in $Li^{3+}+H(1s)$ collisions, as functions of the impact energy E. Theoretical results: Present close-coupling Bessel (—), first Born (……), and STO (---) calculations;———, 3CMO cross sections [10]; □, hydrogenic CTMC cross sections [10]; ∗, 2CAO cross sections [5]; ×, CDW-EIS ionization cross section [57]; +, 1CAO excitation cross sections [30]. Experimental data for capture [69] (▲) and ionization [68] (●). These data have been added to yield the experimental electron-loss cross section (◆).

nicely with previous 1CAO [30], 2CAO [5], 3CMO [10], and hydrogenic CTMC [6] results. In the intermediate $60 \leqslant E \leqslant 200$ keV/amu energy range, the constructed electron-loss cross section of Shah *et al.* [68,69] decays faster with E than the close-coupling and CTMC predictions; as for $He^{2+}+H(1s)$, we attribute this behavior to an eventual underestimation of the experimental ionization cross section around its maximum.

The shapes of STO and Bessel 1CAO results depart from each other for $E \leqslant 60$ keV/amu, despite the use of the same maximum angular momentum $l_{max}=8$ in both bases; even if the differences remain quite small at $E=40$ keV/amu (~9%), it is clear that the shape of the Bessel electron-loss cross section merges better with those of 2CAO, 3CMO, and CTMC calculations than the STO one. This indicates the lack of flexibility of the STO underlying basis to represent the strongly polarized capture flux at low energies.

The CDW-EIS approach [57] provides an ionization cross section in excellent agreement with experiments as soon as $E=200$ keV/amu. Discrepancies occur at lower energies since ionizing transitions via intermediate bound states of the target and projectile are not described within the CDW-EIS framework [57].

We report in Fig. 3(b) our 1CAO and $B1$ $n=2$ and 3 excitation cross sections as functions of E. The $B1$ method leads to accurate predictions for $E \gtrsim 2000$ keV/amu. No significant differences appear between our STO and Bessel 1CAO values. For $E \gtrsim 100$ keV/amu, the lower channel excitation cross sections rather rapidly converge as l_{max} is increased, as shown in Fig. 3(b) by comparison of the 1CAO STO results of Martín with $l_{max}=5$ and ours. Convergence is slower at lower impact energies; nevertheless, $l_{max}=8$ ensures stabilized excitation cross sections (within ~5%) down to $E=40$ keV/amu and our 1CAO results adequately agree in this energy range with the 3CMO calculations of Suárez [70].

Table III contains the excitation and electron-loss cross sections obtained by means of our 1CAO Bessel approach for $40 \leqslant E \leqslant 7000$ keV/amu.

4. Be^{4+}, $B^{5+}+H(1s)$ *collisions*

We report in Figs. 4(a) and 5(a) our 1CAO and $B1$ cross sections for electron loss in $Be^{4+}+H(1s)$) and $B^{5+}+H(1s)$) collisions, respectively. The figures also include the theoretical electron-loss cross sections obtained by means of molecular calculations without pseudostates [33]. In fact, these cross sections refer to the population of the bound molecular orbitals asymptotically correlated to capture; they correspond to genuine capture insofar as ionization is negligible, i.e., in the low impact energy range $E \leqslant 20$ keV/amu. For higher E, the variational character of the method and the dynamical properties of the (fixed-nuclei) molecular orbitals lead to an accumulation of the ionization flux on the highest levels introduced in the expansion [46]. As these are mainly corre-

TABLE III. Cross sections (10^{-17} cm^2) for excitation into $2l$, $3l$, and more excited $n \geqslant 4$ (Rest) levels, and for electron-loss (EL) in $Li^{3+}+H(1s)$ collisions, as functions of the impact energy E. For $E \geqslant 150$ keV/amu, $\sigma_{EL} \sim \sigma_{ion}$ [see Fig. 3(a)].

E (keV/amu)	$n=2$	$2s$	$2p$	$n=3$	$3s$	$3p$	$3d$	Rest	EL
40	12.264	3.9704	8.2931	2.8923	0.7706	1.3936	0.7280	2.7312	164.89
50	15.775	4.3591	11.416	3.6361	0.8344	1.7796	1.0221	3.5376	150.72
75	22.435	4.6987	17.736	5.1250	0.9257	2.8060	1.3932	4.8939	125.03
100	27.412	4.5102	22.902	6.0469	0.9106	3.5714	1.5649	5.6608	105.80
150	31.495	3.8932	27.602	6.6310	0.7976	4.5091	1.3244	6.0146	80.312
200	32.234	3.3348	28.899	6.5854	0.6850	4.8035	1.0969	5.8439	64.918
400	28.087	2.0193	26.068	5.3228	0.4102	4.3868	0.5258	4.5401	36.999
600	23.433	1.4158	22.018	4.2976	0.2856	3.6932	0.3189	3.6072	26.229
800	19.957	1.0845	18.872	3.6056	0.2179	3.1644	0.2234	3.0006	20.541
1000	17.301	0.8723	16.428	3.1058	0.1747	2.7624	0.1687	2.5628	16.905
2000	10.618	0.4386	10.179	1.8654	0.0873	1.7034	0.0747	1.5243	9.2600
5000	5.1493	0.1742	4.9751	0.8903	0.0345	0.8282	0.0276	0.7215	4.1268
7000	3.8638	0.1241	3.7397	0.6697	0.0246	0.6255	0.0195	0.5423	3.0583

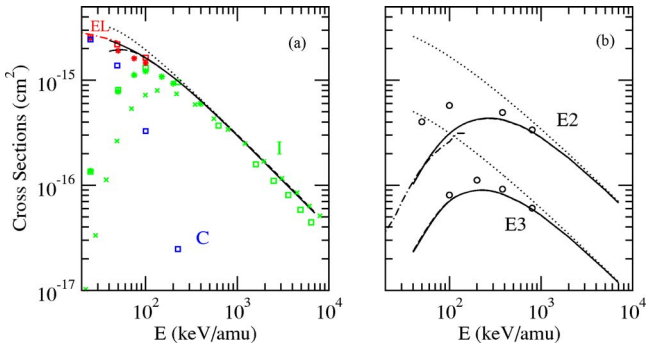

FIG. 4. (Color online) Total ionization (I), capture (C), and electron-loss (EL) (a) and $n=2$ ($E2$) and 3 ($E3$) excitation (b) cross sections in $Be^{4+}+H(1s)$ collisions, as functions of the impact energy E. Theoretical results: Present close-coupling Bessel (—), first Born (……), and STO (---) calculations; □, hydrogenic CTMC cross sections [6];———, molecular electron-loss cross section [33]; ∗, 2CAO cross sections [5]; ×, CDW-EIS ionization cross section [71]; ○, EIA excitation cross sections [8].

lated to capture, one obtains total capture cross sections that correspond to target electron loss.

The molecular electron-loss cross sections are in striking agreement with the 1CAO Bessel ones around 40 keV/amu; this reinforces the complementarity of both approaches to yield accurate cross sections from low to high impact energies. The agreement is also very good with the hydrogenic CTMC calculations of Illescas and Riera [6], and satisfactory with the 2CAO calculations of Toshima [5]. Implementation of the CDW-EIS model by Igarashi and Shirai [71] is successful for $E \geqslant 300$ keV/amu; the maximum of the CDW-EIS ionization cross sections is shifted to higher E with respect to those of 2CAO and hydrogenic CTMC calculations because of the underestimation of ionizing transitions at low E, inherent in the CDW-EIS description.

The inability of the STO expansions to provide accurate electron-loss cross sections at low v, which showed up for the previous collisional systems, is enhanced in the present

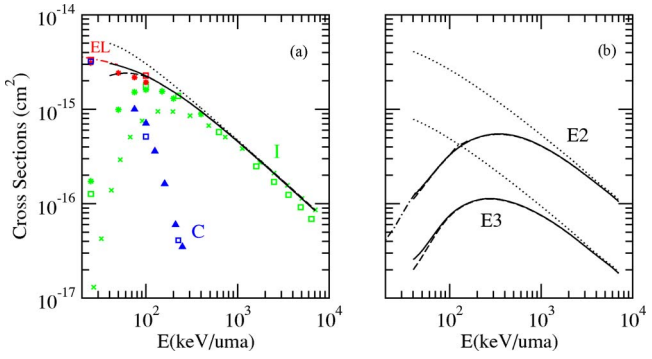

FIG. 5. (Color online) Total ionization (I), capture (C), and electron-loss (EL) (a) and $n=2$ ($E2$) and 3 ($E3$) excitation (b) cross sections in $B^{5+}+H(1s)$ collisions, as functions of the impact energy E. Theoretical results: Present close-coupling Bessel (—), first Born (……), and STO (---) calculations; □, hydrogenic CTMC cross sections [6];———, molecular electron-loss cross section [33]; ∗, 2CAO cross sections [5]. ×, CDW-EIS ionization cross section [71]. Experimental data for capture (▲) [72].

cases with higher projectile charges. The comparison of Figs. 3(a), 4(a), and 5(a) further shows that this liability extends to higher impact energies as the projectile charge increases.

The complementarity of the molecular and Bessel close-coupling approaches also appears in Figs. 4(b) and 5(b), which display the $n=2,3$ excitation cross sections as functions of E. The $B1$ approximation is accurate only for (very) high energies $E \gtrsim 3000$ keV/amu. The EIA approximation fares better at lower E, although significant differences appear between the EIA and 1CAO cross sections for $E \leqslant 500$ keV/amu.

The 1CAO Bessel values of excitation and electron-loss cross sections are given in Tables IV and V for $q=4$ and 5, respectively.

5. $C^{6+}+H(1s)$ *collisions*

Besides 1CAO and $B1$ calculations, we have enlarged for this system our previous molecular calculations [2], in terms of 121 bound orbitals, from low to intermediate ($E=50$ keV/amu) impact energies. The resulting electron-loss cross section is reported in Fig. 6(a), where one can note that the 1CAO Bessel calculations yield an adequate continuation of the molecular cross section to the high impact energy range, as for the previous systems. The STO pseudostates fail in describing the global electron-loss flux as soon as $E \lesssim 100$ keV/amu. Nevertheless, the inelastic total cross sections, i.e., the sum of all bound (with $n \neq 1$) and unbound state populations, obtained by means of the STO and Bessel approaches, are almost identical over the entire impact energy range considered. As the Bessel and STO cross sections to the lower $n=2,3$ channels are practically the same for all E [see Fig. 6(b)], we conclude that a large part of the capture flux is trapped within STO calculations on highly excited *bound* states. We prove this in Fig. 6(a), where we display the respective sums of the STO and Bessel cross sections for excitation into high $n \geqslant 4$ levels: while the sum of Bessel cross sections exhibits an energy dependence similar to those of lower excitation cross sections [see Fig. 6(b)], as may be expected from the Oppenheimer n^{-3} rule [74], which is often employed to extrapolate the cross sections to high n values, the STO sum increases abnormally as the impact energy decreases below $E \lesssim 150$ keV/amu. Moreover, the increase of the $n \geqslant 4$ cross section is found to compensate the decrease of the pseudotate STO cross section so that their sum accurately reproduces (within ~5%) the Bessel (and molecular) electron-loss cross sections. The compensation effect is further demonstrated in Fig. 7(a), where we show, for $E=40$ keV/amu, that the sum of the STO-weighted probabilities $bP(b)$ corresponding to pseudostate population and excitation to $n \geqslant 4$ yields the Bessel electron-loss result.

This mechanism of trapping of the capture flux onto highly excited bound states, which leads to an overestimation of high-n excitation cross sections at low v, exists in all $A^{q+}+H$ systems. Nevertheless, it is more pronounced as q increases because of the growing importance of capture. We have traced back the origin of the trapping to the coarse-grained representation of the target continuum. STO-like underlying sets yield (a few) pseudocontinuum states that rapidly vanish for $r \gtrsim 10$ a.u. because of the exponentially

TABLE IV. Cross sections (10^{-17} cm^2) for excitation into $2l$, $3l$, and more excited $n \geqslant 4$ (Rest) levels, and for electron-loss (EL) in $Be^{4+}+H(1s)$ collisions, as functions of the impact energy E. For $E > 150$ keV/amu, $\sigma_{EL} \sim \sigma_{ion}$ (see Fig. 4(a)).

E (keV/amu)	$n=2$	$2s$	$2p$	$n=3$	$3s$	$3p$	$3d$	Rest	EL
40	10.151	3.7244	6.4264	2.2945	0.7109	1.0499	0.5338	2.3204	239.94
50	14.264	4.4853	9.7790	3.1570	0.7917	1.4801	0.8852	3.1515	222.30
75	23.506	6.0451	17.461	5.4033	1.1079	2.7809	1.5145	5.2075	189.05
100	31.003	6.3500	24.653	7.0443	1.2250	3.8148	2.0045	6.7546	163.52
150	39.030	5.8661	33.164	8.4862	1.1626	5.3140	2.0096	7.8894	128.53
200	42.285	5.1524	37.133	8.9381	1.0313	6.0867	1.8201	8.1111	106.52
400	41.700	3.2770	38.423	8.0975	0.6559	6.4323	1.0092	7.0188	63.511
600	36.781	2.3698	34.411	6.8701	0.4744	5.7626	0.6332	5.8290	45.679
800	32.290	1.8501	30.440	5.9188	0.3702	5.1035	0.4451	4.9637	35.995
1000	28.542	1.5064	27.035	5.1844	0.3012	4.5492	0.3340	4.3030	29.722
2000	18.221	0.7747	17.447	3.2192	0.1543	2.9227	0.1422	2.6374	16.371
5000	9.0406	0.3101	8.7305	1.5660	0.0615	1.4541	0.0504	1.2701	7.3186
7000	6.8104	0.2211	6.5893	1.1818	0.0438	1.1028	0.0353	0.9576	5.4271

decaying r behavior of the basis functions (see Sec. II D). As illustrated in Fig. 7(b), for $E=40$ keV/amu and $b=5$ a.u., such pseudostates are able to describe the polarized capture flux at small intermuclear distances when most of the electronic density is located near the target, but rapidly fail, as $Z=vt$ increases, in reproducing the extension of the density dragged by the projectile. The description of the capture flux then rapidly ends up in terms of excited bound orbitals, which are effectively more diffuse than the pseudostates. This is in contrast with the description provided by Bessel-like effectively complete sets, which yield an accurate enough representation of the continuum states to describe the capture flux by means of target-centered states of positive energy [see Fig. 7(b)]. Nevertheless, even in this description of the electron-loss process, which complies with the requisite of aymptotic positive energy with respect to the target, one cannot separate capture from genuine ionization insomuch as the Bessel basis is unable to represent the peaking of the capture density about the projectile at large internuclear distances.

We finally illustrate in Fig. 8 the convergence of the cross sections obtained by means of the Bessel 1CAO approach with respect to the key parameters of the basis, r_{max} and l_{max}. It is worth noting that within 1CAO frameworks, convergence is harder to reach as the projectile charge increases, because of the growing importance of capture whose description requires high values of l_{max}; this is why we have chosen to present our convergence checks for the most demanding $C^{6+}+H(1s)$ case. For fixed l_{max}, the excitation cross sections are insensitive to the decrease of r_{max} (from 100 to 60 a.u. in Fig. 8), as long as the corresponding bound states remain entirely described within the reduced box. The electron-loss cross section, which corresponds to pseudocontinuum state population, also remains unchanged under variation of r_{max}; this stability complements from a dynamical point of view the (static) criterion for effective completeness of the Bessel

TABLE V. Cross sections (10^{-17} cm^2) for excitation into $2l$, $3l$, and more excited $n \geqslant 4$ (Rest) levels, and for electron-loss (EL) in $B^{5+}+H(1s)$ collisions, as functions of the impact energy E. For $E > 150$ keV/amu, $\sigma_{EL} \sim \sigma_{ion}$ [see Fig. 5(a)].

E (keV/amu)	$n=2$	$2s$	$2p$	$n=3$	$3s$	$3p$	$3d$	Rest	EL
40	12.034	5.2696	6.7644	2.5549	0.8366	1.1631	0.5551	2.4392	306.45
50	15.112	5.5355	9.5769	3.1814	0.9298	1.4443	0.8073	2.9423	290.08
75	24.002	7.1717	16.830	5.4078	1.2885	2.6894	1.4299	5.1562	255.45
100	32.731	7.8672	24.864	7.4974	1.4953	3.8384	2.1637	7.2707	225.70
150	44.144	7.8943	36.250	9.8735	1.5565	5.7432	2.5738	9.3702	181.77
200	50.033	7.2414	42.792	10.929	1.4480	6.9524	2.5283	10.134	153.19
400	54.439	4.7922	49.647	10.826	0.9510	8.2705	1.6042	9.5308	94.814
600	50.375	3.5129	46.862	9.5835	0.6973	7.8334	1.0528	8.2190	69.314
800	45.497	2.7731	42.724	8.4647	0.5515	7.1608	0.7524	7.1547	55.070
1000	40.994	2.2784	38.715	7.5389	0.4536	6.5180	0.5673	6.2957	45.691
2000	27.292	1.1975	26.095	4.8528	0.2384	4.3768	0.2376	3.9871	25.383
5000	13.907	0.4846	13.423	2.4144	0.0962	2.2373	0.0809	1.9602	11.399
7000	10.527	0.3458	10.181	1.8297	0.0686	1.7049	0.0561	1.4836	8.4602

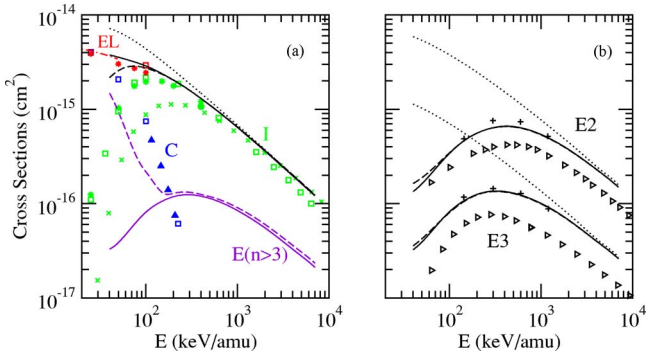

FIG. 6. (Color online) Total ionization (I), capture (C), and electron-loss (EL) (a) and $n=2$ ($E2$) and 3 ($E3$) excitation (b) cross sections in $C^{6+}+H(1s)$ collisions, as functions of the impact energy E. Theoretical results: Present close-coupling Bessel (—), first Born (……), and STO (---) calculations; □, hydrogenic CTMC cross sections [6];—·—·—, molecular electron-loss cross section [2]; ∗, 2CAO cross sections [5]; ×, CDW-EIS ionization cross section [71]; ▷, microcanonical CTMC excitation cross sections; +, 1CAO excitation cross sections [30]. Experimental data for capture (▲) [72,73] and ionization (●) [73]. In (a), the curves (—) and (---) labeled $E(n>3)$ correspond to the respective sums of Bessel and STO $n\geqslant 4$ excitation cross sections.

set within the box, which is based on the coincidence of computed and expected densities of pseudocontinuum box modes (see Sec. II D and [32]). For a fixed box size, we show in Fig. 8 how weak the changes are in both electron-loss and excitation cross sections when l_{max} varies from 6 to 8; our larger $l_{max}=8$ basis ensures converged results, within less than 10%, over the whole impact energy range $40\leqslant E\leqslant 7000$ keV/amu, even for the higher excitation levels considered ($n=6$).

Table VI compiles the excitation and electron-loss cross sections provided by the Bessel 1CAO calculations.

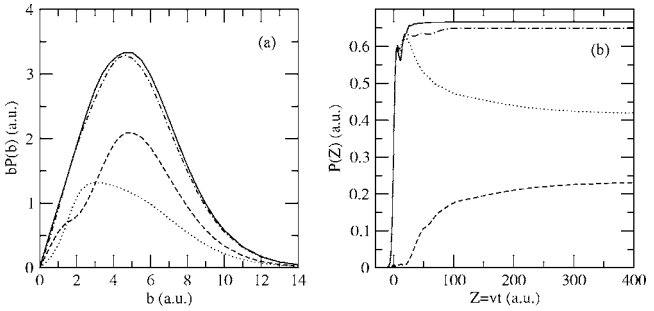

FIG. 7. (a) Weighted probabilities for pseudostate population $bP_{ion}^{cc,STO}(v,b,t_{max})$ (…), excitation to $n\geqslant 4$ levels $bP_{n\geqslant 4}^{cc,STO}(v,b,t_{max})$ (---), and $bP_{ion}^{cc,STO}(v,b,t_{max})+bP_{n\geqslant 4}^{cc,STO}(v,b,t_{max})$ (-·-·-) obtained by means of our 1CAO STO calculations for $C^{6+}+H(1s)$ collisions at $E=40$ keV/amu, compared to the electron-loss (pseudostate) $bP_{ion}^{cc,Bessel}(v,b,t_{max})$ weighted probability (—) obtained by means of our 1CAO Bessel calculations. (b) Temporal evolution of $P_{ion}^{cc,STO}(v,b,t)$ (…), $bP_{n\geqslant 4}^{cc,STO}(v,b,t)$ (---), $P_{ion}^{cc,STO}(v,b,t)+P_{n\geqslant 4}^{cc,STO}(v,b,t)$ (-·-·-) , and $bP_{ion}^{cc,Bessel}(v,b,t)$ (—) as a function of scaled time $Z=vt$ in $C^{6+}+H(1s)$ collisions for $E=40$ keV/amu and $b=5$ a.u.

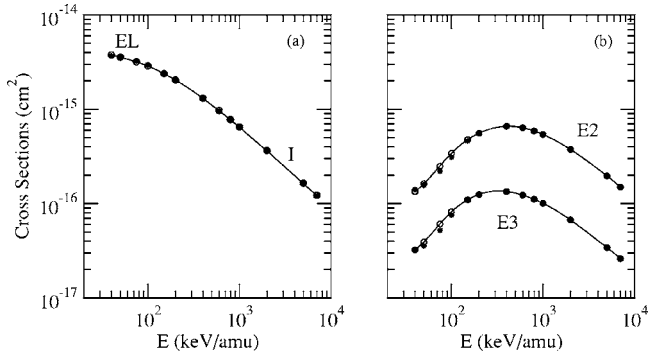

FIG. 8. Convergence of electron-loss (a) and $n=2$ ($E2$) and 3 ($E3$) excitation (b) cross sections obtained by means of Bessel 1CAO calculations for $C^{6+}+H(1s)$ collisions, with respect to values of r_{max} and l_{max}: (—), $\{r_{max}=100,\ l_{max}=8,\ k_{max}=2.5\}$ basis; ○, $\{r_{max}=60,\ l_{max}=8,\ k_{max}=2.5\}$ basis; ∗, $\{r_{max}=100,\ l_{max}=6,\ k_{max}=2.5\}$ basis.

B. Scaling rules for excitation partial cross sections

As stated in the Introduction, H or D neutral beams of intermediate energies are commonly injected into Tokamak plasma devices for diagnostic purposes. The excitation processes of such neutral atoms in collisions with typical plasma impurities of charge $q\leqslant 6$ are especially efficient in the intermediate impact energy domain (see Figs. 1–6). The corresponding collisional rates, which are derived directly from the cross sections through integration over the temperature distribution, have thus to be included in the balance equations used to model the diagnostic. In this respect, we believe that our 1CAO Bessel calculations are of great interest. Nevertheless, heavy species may be desorbed from the coated walls and reach an ionization stage higher than 6 as they approach the plasma core; one may also be interested in excitation to high-lying atomic states, beyond the scope of our present Bessel calculations whose reliability is restricted to $n\leqslant 6$ because of $r_{max}=100$ a.u. (see Sec. II D). One thus easily understand the importance of deriving, as far as possible, analytical scaling relations for $A^{q+}+H(1s)\rightarrow A^{q+}+H(nl)$ reactions, as functions of q, E, and $|E_1-E_n|$ transition energy.

The derivation of our scaling rules is similar to that of Janev [34], who used the advanced adiabatic approach to low-energy ion-atom collisions [75] and the dipole close-coupling [37] and classical impulse [36] approximations (for optically allowed and optically forbidden transitions, respectively) for intermediate to high impact energies to show that the $A^{q+}+H(1s)\rightarrow A^{q+}+H(np)$ cross sections should obey the scaling relationship

$$\tilde{\sigma}_p(\tilde{E})=\frac{\omega_{1n}^2}{qf_{1n}}\sigma_{np}(E),\quad \tilde{E}=\frac{E}{q\omega_{1n}},\tag{13}$$

whereas optically forbidden transitions $A^{q+}+H(1s)\rightarrow A^{q+}+H(nl)$ with $l\neq 1$ should lead to cross sections that scale according to

$$\tilde{\sigma}_{l\neq 1}(\tilde{E})=\frac{n^3\omega_{1n}^4}{q}\sigma_{nl}(E),\quad \tilde{E}=\frac{E}{q\omega_{1n}}.\tag{14}$$

In the two previous equations, $\omega_{1n}=|E_1-E_n|$ is expressed in a.u. and f_{1n} is the oscillator strength [76].

TABLE VI. Cross sections (10^{-17} cm^2) for excitation into $2l$, $3l$, and more excited $n \geqslant 4$ (Rest) levels, and for electron-loss (EL) in C^{6+}+H($1s$) collisions, as functions of the impact energy E. For $E > 150$ keV/amu, $\sigma_{EL} \sim \sigma_{ion}$ [see Fig. 6(a)].

E (keV/amu)	$n=2$	$2s$	$2p$	$n=3$	$3s$	$3p$	$3d$	Rest	EL
40	13.404	6.4353	6.9684	3.2418	0.9199	1.6470	0.6749	3.2999	376.17
50	16.212	6.7341	9.4784	3.9150	1.2512	1.8250	0.8388	3.8619	356.01
75	24.845	8.2647	16.580	6.0848	1.6321	2.9956	1.4571	6.0087	319.11
100	34.089	9.1142	24.975	8.2010	1.8118	4.0841	2.3051	8.1219	287.38
150	47.613	9.4639	38.149	10.964	1.8813	6.0532	3.0296	10.590	237.93
200	55.760	9.0613	46.699	12.512	1.8204	7.5314	3.1602	11.833	203.93
400	65.958	6.4892	59.469	13.413	1.2904	9.8482	2.2745	11.995	130.05
600	63.604	4.8402	58.764	12.318	0.9579	9.7994	1.5607	10.678	96.446
800	58.906	3.8511	55.055	11.122	0.7625	9.2211	1.1382	9.4751	77.269
1000	54.017	3.1831	50.834	10.059	0.6311	8.5611	0.8667	8.4521	64.456
2000	37.483	1.7024	35.781	6.7102	0.3385	6.0084	0.3633	5.5301	36.192
5000	19.661	0.6973	18.964	3.4221	0.1385	3.1635	0.1201	2.7817	16.350
7000	14.965	0.4984	14.466	2.6058	0.0989	2.4244	0.0825	2.1146	12.148

We have used our most accurate σ_{nl} values, i.e., those previously obtained by means of the 1CAO Bessel approach for $1 \leqslant q \leqslant 6$, $2 \leqslant n \leqslant 6$, and $40 \leqslant E \leqslant 7000$ keV/amu, to plot in Fig. 9 the scaled cross sections $\tilde{\sigma}_l(\tilde{E})$ as functions of the reduced energy $\tilde{E}$. To improve the concord of $\tilde{\sigma}_{l\neq 1}(\tilde{E})$ scaled results on (l-dependent) universal curves (see Fig. 9), it has been necessary to multiply all the σ_{20}, σ_{32}, and σ_{43} cross sections by 1.15, 1.4, and 1.8, respectively; the first excitation subshell (with $n=l+1$ for $l \neq 0$ and $n=2$ otherwise) thus does not strictly fulfill the scaling law (13). This is consistent

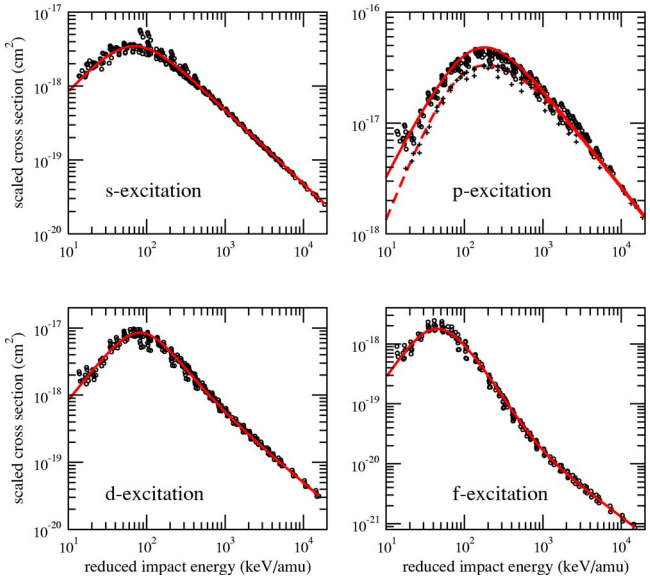

FIG. 9. (Color online) Scaling rules (—) for excitation cross sections into s, p, d, and f states in A^{q+}+H($1s$) collisions, corresponding to Eqs. (15)–(18), respectively. (---) corresponds to the scaling rule (19) for $1s \rightarrow 2p$ transitions. (○) and (+) refer to explicit 1CAO Bessel calculations for the processes A^{q+}+H($1s$) $\rightarrow A^{q+}$+H(nl) with $2 \leqslant n \leqslant 6$ and $1 \leqslant q \leqslant 6$ (+ symbols are used to differentiate the $2p$ cross sections).

with the condition $n \gg 1$ that has been assumed in both the advanced adiabatic and classical impulse approaches to obtain the simple parametrization (13) [34]; $n \gg 1$ results in the fulfillment of the n^{-3} Oppenheimer rule [see Eq. (13)], which is known to be inaccurate for the lowest shells as shown, e.g., in [10] for capture. As we now deal with (n,l) subshell populations, $n > l+1$ is an additional (and more precise) requisite to the validity of the relationship (13).

The $n > l+1$ criterion also holds for the optically allowed transitions since the $2p$ reduced cross sections clearly depart from the common behavior of other np scaled results for $\tilde{E} \lesssim 1000$ keV/amu (see Fig. 9). The merging of all the np reduced cross sections over the whole $\tilde{E}$ range cannot be improved as before by introducing an empirical factor for the $2p$ results, insomuch as all the np scaled cross sections suitably coalesce for $\tilde{E} \gtrsim 1000$ keV/amu according to the dipole close-coupling model in which the condition $n \gg 1$ has not been used. It is preferable, for the sake of accuracy, to consider separately the $2p$ and np ($n \neq 2$) scaling behaviors.

For practical purposes, we have fitted the $\tilde{\sigma}_l(\tilde{E})$ universal curves of Fig. 9 to the following analytical functions (in units of 10^{-17} cm^2):

$$\tilde{\sigma}_0(\tilde{E}) = \frac{10}{3100\tilde{E}^{-1.3}e^{0.82/\sqrt{\tilde{E}}} + 0.21\tilde{E}}, \tag{15}$$

$$\tilde{\sigma}_{1,n\neq 2}(\tilde{E}) = \frac{10\ln(e+\tilde{E})}{450\tilde{E}^{-0.9}e^{1/\sqrt{\tilde{E}}} + 0.035\tilde{E}}, \tag{16}$$

$$\tilde{\sigma}_2(\tilde{E}) = \frac{10}{2050\tilde{E}^{-1.35}e^{0.82/\sqrt{\tilde{E}}} + 0.2\tilde{E}^{1-\exp(-0.25\tilde{E}^{0.4})}}, \tag{17}$$

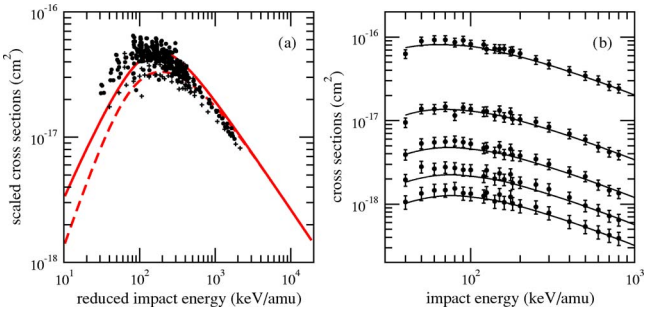

FIG. 10. (Color online) (a) (○) and (+) refer to the experimental data of Detleffsen *et al.* [77] for ion-induced $H(1s) \rightarrow H(np)$ transitions (+ symbols are used to differentiate the $2p$ cross sections). (—) and (---) are the scaling rules (16) and (19). (b) (●), $H^+ + H(1s) \rightarrow H^+ + H(np)$ cross sections of Detleffsen *et al.* with n ranging from 2 (top) to 6 (bottom); (—) corresponding 1CAO Bessel results.

$$\tilde{\sigma}_3(\tilde{E}) = \frac{1.3}{2200\tilde{E}^{-1.8}e^{0.82/\sqrt{\tilde{E}}} + \tilde{E}^{1-\exp(-0.052\tilde{E}^{0.6})}}, \qquad (18)$$

where $e=2.718282$ has been introduced in the logarithmic argument of Eq. (16) to avoid negative values for $\tilde{E}<1$. All these functions behave as $\exp(-a\tilde{E}^{-1/2})$ at low $\tilde{E}$, where a is a positive constant, in accordance with the prescriptions of the simplified implementation of the adiabatic approach in terms of Q superseries [34]. In the high $\tilde{E}$ energy region, $\tilde{\sigma}_1$ and $\tilde{\sigma}_{l\neq 1}$ present, respectively, the $\ln\tilde{E}/\tilde{E}$ and $1/\tilde{E}$ Born shapes. Nevertheless, for $l=2$ and 3, the first-order $1/\tilde{E}$ behavior is observed for $\tilde{E} \gtrsim 1000$ and 2000 keV/amu, respectively, far beyond the maximum of the reduced cross sections (see Fig. 9); this denotes the existence of important higher-order transitions in the intermediate $100 \lesssim \tilde{E} \lesssim 1000$ keV/amu regime. This effect has been incorporated in our functions (17) and (18) through the exponential factors in the denominators that delay the fulfilment of the $1/\tilde{E}$ behavior. For the special case of $1s \rightarrow 2p$ transitions, we prescribe the use of the scaling function,

$$\tilde{\sigma}_{1,n=2}(\tilde{E}) = \frac{10\ln(e+\tilde{E})}{2900\tilde{E}^{-1.3}e^{0.8/\sqrt{\tilde{E}}} + 0.035\tilde{E}^{1+\exp(-0.26\tilde{E}^{0.4})}}, \qquad (19)$$

which smoothly tends to $\tilde{\sigma}_{1,n\neq 2}(\tilde{E})$ for $\tilde{E} \gtrsim 1000$ keV/amu as expected.

The experimental data of Detleffsen *et al.* [77] for $1s \rightarrow np$ excitation of H, with $n=2-6$, induced by H^+, He^+, He^{2+}, Si^{q+} ($q=2-9$), and Cu^{q+} ($q=3-11$) ion impact are presented in Fig. 10(a) in the reduced representation (13). Our scaling functions (16) and (19) adequately reproduce the whole data within the experimental uncertainties which are of the order of 40% for the higher sublevels and heavier species considered. The deviations are stronger in the low $\tilde{E}$ range, and the H^+ data systematically lie 15% below our $\tilde{\sigma}_1(\tilde{E})$ curve, as may be seen in Fig. 10(a), where the experimental points for $\tilde{E} \geqslant 500$ keV/amu only concern H^+ impact. Our 1CAO Bessel results for H^+ collisions also lie ~15% below the fits (16) and (19) for $\tilde{E} \lesssim 2000$ keV/amu, and present good agreement with the measurements of Detleffsen *et al.*, as shown in Fig. 10(b). Previous studies on the pertinence of scaling relations for excitation in $A^{q+}+He$ collisions have shown that the cross sections for proton impact differ from a common curve for multiply charged ions [78,79]. In the present case with H target, the H^+ impact singularity is small but the deviations of our computed cross sections with respect to the fits (16) and (19), and to Eqs. (15)–(19) in general, are indeed even smaller for multicharged ($q \geqslant 2$) ion impact. We thus claim that these relations can be safely used, taking into account the above-mentioned multiplicative factors for σ_{20}, σ_{32}, and σ_{43} cross sections, in the fusion context whenever more accurate theoretical and/or experimental data do not exist.

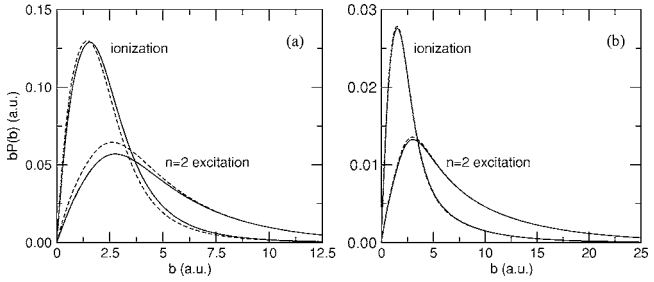

FIG. 11. Weighted ionization and $n=2$ excitation probabilities $bP(b)$ in $H^+ + H(1s)$ collisions, as functions of the impact parameter b, for impact energies $E=200$ (a) and 1000 keV/amu (b): close-coupling Bessel calculations (—); first-Born Bessel results (---).

C. Comparison of close-coupling and perturbative descriptions of the ionization process

We now turn to a comparative analysis of the close-coupling and perturbative $B1$ descriptions of the ionization process, as described in Sec. II C. This comparison will be drawn for $H^+ + H$ benchmark, in the impact energy region where the $B1$ approach leads to accurate ionization total cross sections and where capture, which accumulates on target-centered pseudostates, can be neglected, i.e., for $E \geqslant 200$ keV/amu [see Fig. 1(a)].

We first show in Fig. 11 that the agreement of the close-coupling and $B1$ total cross sections also holds for the weighted ionization probabilities $bP_{\rm ion}^{\rm cc,B1}$ for $E \geqslant 200$ keV/amu. As may be expected, $P_{\rm ion}^{\rm cc}$ and $P_{\rm ion}^{B1}$ better merge as E increases. So all the following analysis will refer to $E=1000$ keV/amu, where $bP_{\rm ion}^{\rm cc,B1}$ are almost identical over the whole b range, although we have checked the validity of our next illustrations for all $E \geqslant 200$ keV/amu.

The temporal evolution of the ionization (and excitation) probabilities is displayed in Fig. 12 as a function of scaled time $Z=vt$, for a (representative) nuclear trajectory with $b=1.5$ a.u. leading to maximum $bP_{\rm ion}^{\rm cc,B1}$. The ionization close-coupling and perturbative probabilities are in close agreement throughout the collision, and depict ionization as a relatively fast process whereby the electron becomes

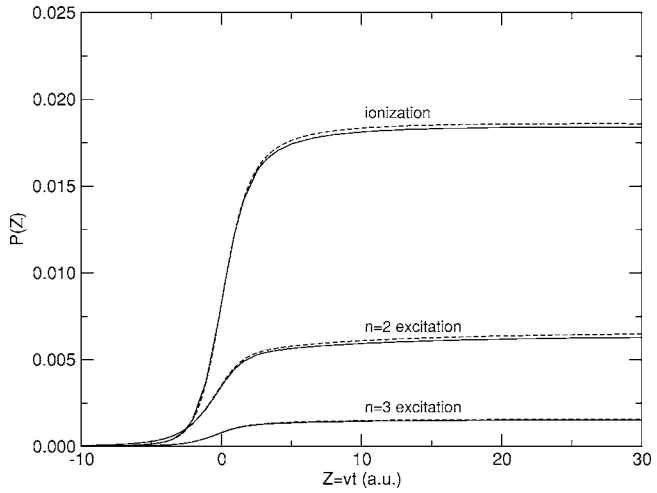

FIG. 12. Temporal evolution of the ionization and excitation probabilities in $H^+ + H(1s)$ collisions for a nuclear trajectory with impact velocity $v=6.325$ a.u. and impact parameter $b=1.5$ a.u., as a function of the nuclear coordinate $Z=vt$ (same symbols as in Fig. 10).

unbound around $Z=0$ a.u., when the projectile crosses the target. It is noteworthy that even for $b \gg 1$ a.u., where the electron-projectile interaction is of a dipolar nature for all Z, most of the ionizing events occur from $Z=-10$ to $Z=10$ a.u.

We now go deeper into the $B1$ description of the ionization dynamics and present in Fig. 13 time samplings of the one-dimensional transverse $\rho_{\text{ion}}^{B1}(p_x,v,b,t)$ and longitudinal $\rho_{\text{ion}}^{B1}(p_z,v,b,t)$ momentum distributions, obtained by integrating $|\Psi_{\text{ion}}^{B1}(\mathbf{p},v,b,t)|^2$ over the remaining variables with $\hat{\mathbf{p}}_\mathbf{x}=\hat{\mathbf{b}}$ and $\hat{\mathbf{p}}_\mathbf{z}=\hat{\mathbf{v}}$. These distributions are compared to their close-coupling 1CAO counterparts. It is clear from the figure that the $B1$ and 1CAO calculations yield similar ejected electron distributions throughout the collision. The salient feature of the sampling is the rapid formation of a $p\pi$-shaped ionizing density (see Fig. 13 at $Z=10$ a.u.), which is consistent with an approximate sudden description of the ionization process at $Z=0$ a.u. where the electron-projectile interaction is reduced to the dipolar (x/b^2) force in the $\hat{x}$ direction, yielding $1s \rightarrow p\pi$ transitions in the laboratory-fixed frame of reference. As time elapses further ($Z>10$ a.u.), the π symmetry of the cloud vanishes and $\sim 60\%$ of the ionized electrons are finally emitted in the negative transverse direction. For $Z \geqslant 200$ a.u., we enter into the asymptotic region where the momentum distributions no longer change significantly; this emphasizes the long-range influence of the Coulomb post-collisional effects since the ionization probability reached its asymptotic value much earlier, around $Z=10$ a.u. Nevertheless, weak changes are observed for $Z \geqslant 50$ a.u., mainly consisting of a narrowing of the distributions about the $(p_x=0, p_z=0)$ target nucleus.

To better understand the ionization dynamics, we make use of the symmetry about the (x,z) collisional plane and report in Fig. 14 the close-coupling and $B1$ velocity diagrams $\{\mathbf{r},\mathbf{v}_\mathbf{e}^{\text{cc},B1}\}$ as defined in Sec. II C, for the ionizing electrons that lie about $y=0$ a.u. The velocity fields are only drawn in the space regions where $\rho_{\text{ion}}^{\text{cc},B1}(x,z,v,b,t) \geqslant \rho_{\text{ion}}^{(\text{cc},B1)_{\max}}/10$, with $\rho_{\text{ion}}^{(cc,B1)_{\max}}$ the maximum ionizing density in the $y=0$ plane. The first velocity diagrams correspond to $Z=-2$ a.u. and show how ionization arises from a drift of the cloud toward the projectile; the ionizing density is accordingly strongly polarized along the internuclear axis and exhibits a $p\sigma$ shape in the rotating frame of reference, as discussed above. The comparison of the close-coupling and $B1$ diagrams shows that the polarization is weaker within the $B1$

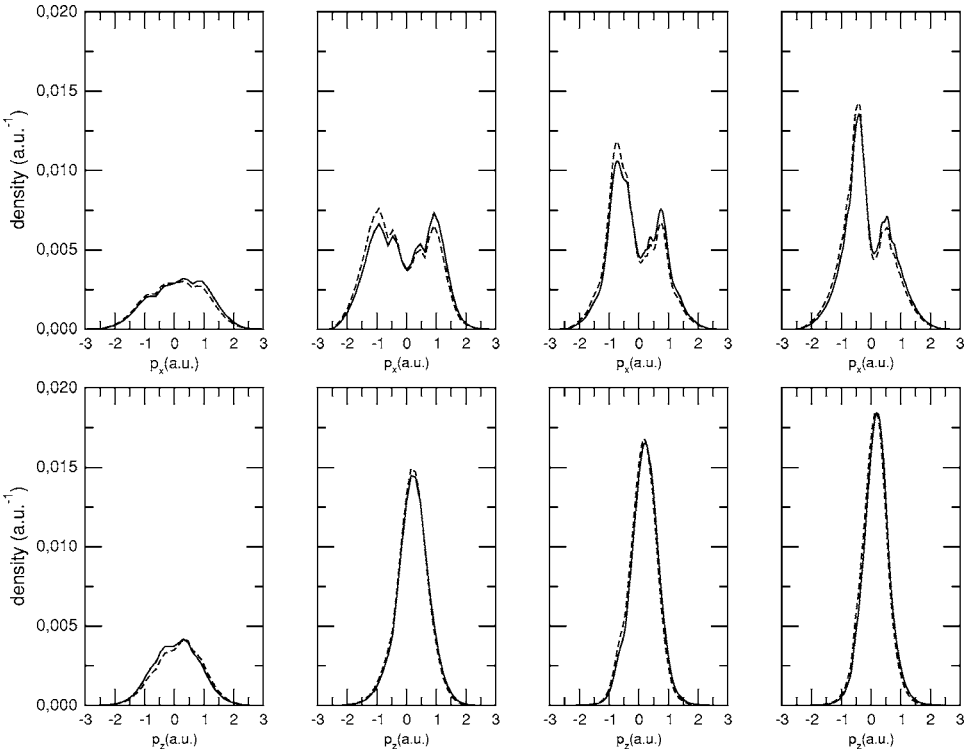

FIG. 13. Transverse (top) and longitudinal (bottom) electronic ionizing distributions in momentum space, for $H^+ + H(1s)$ collisions along the nuclear trajectory with $v=6.325$ a.u., $b=1.5$ a.u., and $vt=0$, 10, 50, and 200 a.u. Close-coupling (—) and first-Born (…) Bessel calculations.

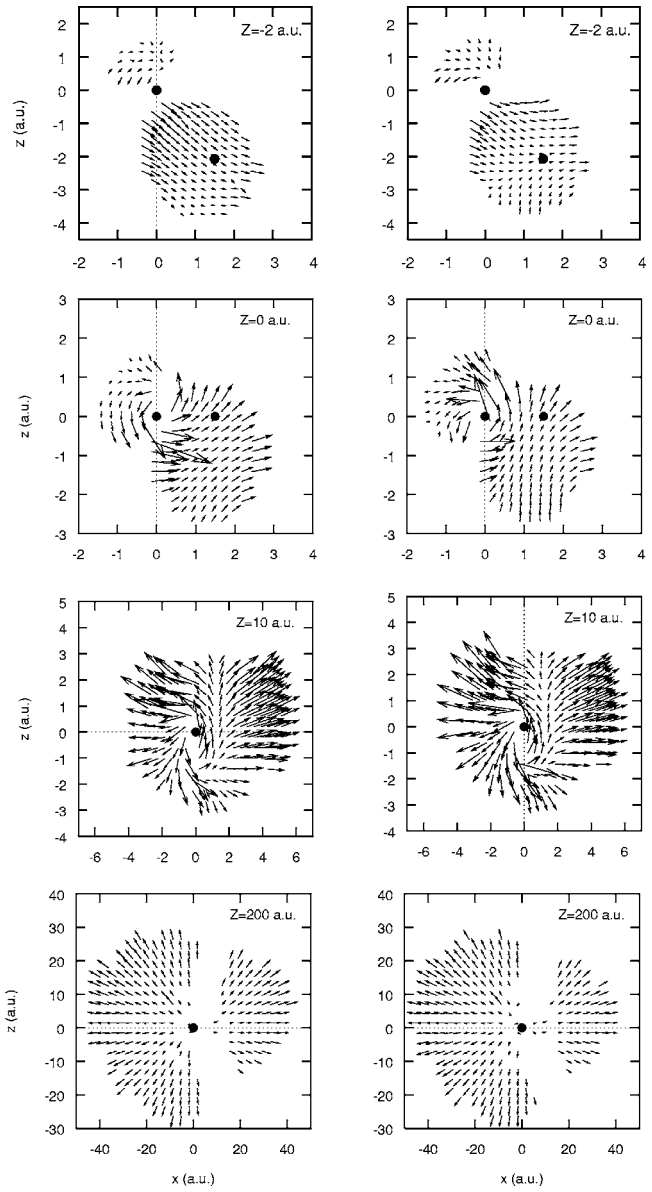

FIG. 14. Close-coupling (left) and $B1$ perturbative (right) velocity diagrams $\{\mathbf{r},\mathbf{v_e}\}$ for the ionizing electrons that lie about the collision plane in $H^+ + H(1s)$ collisions, along the nuclear trajectory with $v=6.325$ a.u. and $b=1.5$ a.u. The velocity vectors are multiplied by the scaling factor $l=1$, 1, 1, and 4 a.u. for $Z=-2$, 0, 10, and 200 a.u., respectively. The nuclear positions are indicated (●).

framework so that $v_e^{B1} < v_e^{cc}$ in the vinicity of the projectile [notwithstanding that $P_{ion}^{B1}(Z=-2)=P_{ion}^{cc}(Z=-2)$ in Fig. 12]. As the projectile crosses the target, new ionizing events occur (both P_{ion}^{B1} and P_{ion}^{cc} increase around $Z=0$ a.u. in Fig. 12) as a result of the polarization effect. The 1CAO and $B1$ ionization fluxes are laminar, except (very) close to the scattering nuclear centers where electrons are strongly accelerated. The $B1$ approximation still understates the drifting influence of the projectile and $\mathbf{v}_{e_x}^{cc} > \mathbf{v}_{e_x}^{B1}$ for the electrons that are left behind the projectile. This discrepancy is slightly visible in the $Z=0$ a.u. momentum distributions of Fig. 13, where $\rho_{ion}^{cc}(p_x) \gtrsim \rho_{ion}^{B1}(p_x)$ for $p_x > 0$; nevertheless, it does not have important consequences of the subsequent evolution of the ionizing cloud: the projectile is so swift with respect to the ionized electrons ($v_e^{cc,B1} \ll v$) so that as soon as they are ionized, outer electrons ($x > b$) are accelerated in the positive transverse direction while the inner ones ($x < b$) are strongly deflected by the target in the $p_x < 0$ direction. This wake effect is illustrated in Fig. 14 for $Z=10$ a.u.. In $B1$ calculations, the initial weaker shift of the electrons toward the projectile results in a slightly more pronounced deflection by the target and $\rho_{ion}^{B1}(p_x) \lesssim \rho_{ion}^{cc}(p_x)$ for $p_x > 0$ in Fig. 13. As time elapses further, the electrons, which remain relatively close to the target, are mainly subject to the attraction of this latter and are accordingly decelerated, yielding the above-mentioned narrowing to the momentum distributions about $\mathbf{p}=\mathbf{0}$. They finally reach a stationary state when the projectile-electron interaction can be effectively neglected.

The last $B1$ velocity diagram of Fig. 14 is almost identical to the close-coupling one, and all of them exhibit an isotropic expansion of the ionized cloud, in which the $\mathbf{r}$ and $\mathbf{v}_e^{cc,B1}$ vectors point at the same direction. It can be further checked that so that the perturbative approach confirms that when viewed from the asymptotic region, the ionization mechanism appears as a quasifree expansion from the target-centered region. The $B1$ ionization wave function Ψ_{ion}^{B1} accordingly presents all the characteristics detailed in [40] for $t \gg 0$: its phase reduces to the "explosive" one $S(\mathbf{r},t)=r^2/2t$ in configuration space and to $p^2t/2$ in momentum space, the corresponding momentum distributions rapidly become stationary (see Fig. 13 for $Z \gtrsim 50$ a.u.), and $\mathbf{r}$ and $\mathbf{p}$ distributions are soon related by $\rho_{ion}(\mathbf{r},v,b,t) \sim \rho_{ion}(\mathbf{p}t,v,b,t)$; all these properties, which directly follow from the mechanism, are not detailed herein for the sake of conciseness. We finally conclude that all existing theoretical methods, when optimized so as to accurately describe ionization [32,40], i.e., classical CTMC [39], semiclassical 2CAO [41], 1CAO [31], and perturbative $B1$, support the quasifree expansion process as the main ionization mechanism in atomic collisions. This definitively establishes its truthfulness.

IV. CONCLUSIONS

We have performed monocentric close-coupling calculations to obtain partial and total cross sections for excitation and electron-loss in bare $A^{q+} + H(1s)$ collisions, with $1 \leqslant q \leqslant 6$, from intermediate ($E=40$ keV/amu) to high ($E=7000$ keV/amu) impact energies.

We first employed a large-scale 1CAO expansion in terms of (standard) even-tempered STO's. We have shown that such an expansion yields inaccurate, overestimated, cross sections for excitation to high-lying bound states at low E. This failure is related to a contamination of the excited bound levels by the capture flux, and is therefore more pronounced and extents to higher impact energies as q increases. The capture flux should be described, according to the variational character of the method and because of the asymptotic dynamical properties of a captured electron, in terms of continuum target eigenstates. But the discretized STO description of the atomic continuum, which consists of a few short-range pseudostates, rapidly becomes inadequate to represent

the polarized capture flux in the outgoing stage of the collision. The propagation of the flux is then biased, as explained in [47], and finally evolves toward diffuse bound states, efficiently coupled to the pseudostates. This wrong behavior can be obviously weakened by using geometrical series $\{\alpha_0,\beta,j_{\max}\}$ with α_0 so large as not to provide Rydberg states through diagonalization of the target Hamiltonian; nevertheless, this procedure leads to a worse description of the continuum, and the contamination of lower states with $n\sim 4$ never totally disappears at low impact energies.

We thus employed an optimized 1CAO approach, in terms of confined spherical Bessel functions, which is known to provide an accurate and dense enough description of the continuum and a reliable description of the ionization process [27,31,32]. We have obtained well-behaved excitation cross sections for all collisional systems, and ionization cross sections which accurately correspond to the target electron-loss (capture+ionization) flux at low E, as expected. Furthermore, all these cross sections suitably coalesce with their molecular counterparts around $E=40$ keV/amu, so that the merging of our molecular and Bessel 1CAO approaches yields accurate cross sections for the main collisional processes from low to high impact energies. We finally checked that the 1CAO Bessel results accurately tend to the first Born perturbative ones in the high-energy limit.

For application purposes such as plasma modeling, we have derived from our calculations the semiempirical scaling rules (15)–(19) for s-, p-, d- and f-excitation cross sections. We have shown, by means of comparison with experimental data, that these relationships, which depend on the impact energy, projectile charge, and electron transition energy, can be safely used in applications whenever more accurate theoretical and/or experimental data do not exist. In the case of complicated systems with inert core electrons on the projectile, the usual (and simple) effective charge approximation is advisable. It has to be reminded that the σ_{20}, σ_{32}, and σ_{43} cross sections derived from Eqs. (15)–(19) have to be respectively scaled by the inverse of the empirical factors 1.15, 1.4, and 1.8, which have been introduced in the merging of our computed cross sections to counteract the n^{-3} Oppenheimer rule that does not apply for small n.

Finally, we have undertaken impact parameter first-Born calculations using spherical Bessel functions to show that they bear out the classical [39] and semiclassical [27,31,40,41] quasifree expansion pictures of the ionization process. In our time-dependent analysis of ionizing densities and velocity fields, we showed that the $B1$ treatment locally understates the polarization induced by the projectile at small internuclear distances; nevertheless, in the high impact velocity region where $B1$ applies, this does not have important consequences on the subsequent evolution of the ionizing cloud so that the close-coupling and $B1$ descriptions closely agree in the asymptotic region. Furthermore, higher-order perturbative treatments such as CDW-EIS (continuum distorted wave–eikonal initial state) [57,80] are bound to be successful in meeting with the local discrepancy at small R while still corroborating the quasifree expansion picture.

ACKNOWLEDGMENTS

This work has been partially supported by DGICYT projects FIS2004-04145 and ENE2004-06266/FTN. We would like to acknowledge the Ministerio de Ciencia y Tecnología (Spain) and the Ministère des Affaires Etrangères (France) for financial support under the coordinated program AIHF04-Picasso2004, and the computational facilities provided with the M3PEC scientific pole of intensive numerical calculations, a member of the DRIMM at the University of Bordeaux–I.

[1] H. P. Summers *et al.*, Plasma Phys. Controlled Fusion **44**, B323 (2002).
[2] C. Harel, H. Jouin, and B. Pons, At. Data Nucl. Data Tables **68**, 279 (1998).
[3] D. Belkic, R. Gayet, and A. Salin, At. Data Nucl. Data Tables **51**, 76 (1992).
[4] R. C. Isler, Plasma Phys. Controlled Fusion **36**, 171 (1994).
[5] N. Toshima, Phys. Rev. A **50**, 3940 (1994).
[6] C. Illescas and A. Riera, Phys. Rev. A **60**, 4546 (1999).
[7] D. J. W. Hardie and R. E. Olson, J. Phys. B **16**, 1983 (1983).
[8] V. D. Rodriguez and J. E. Miraglia, J. Phys. B **25**, 2037 (1992).
[9] L. F. Errea, C. Harel, C. Illescas, H. Jouin, L. Méndez, B. Pons, and A. Riera, J. Phys. B **31**, 3199 (1998).
[10] L. F. Errea, C. Illescas, L. Méndez, B. Pons, A. Riera, and J. Suárez, J. Phys. B **37**, 4323 (2004).
[11] T. G. Winter and C. D. Lin, Phys. Rev. A **29**, 3071 (1984).
[12] B. M. McLaughin, T. G. Winter, and J. F. McCann, J. Phys. B **30**, 1043 (1997).
[13] N. Toshima, Phys. Rev. A **59**, 1981 (1999).
[14] H. A. Slim and A. Ermolaev, J. Phys. B **27**, L203 (1994).
[15] J. Kuang and C. D. Lin, J. Phys. B **29**, 1207 (1996).
[16] J. Kuang and C. D. Lin, J. Phys. B **30**, 101 (1997).
[17] H. J. Lüdde, A. Henne, T. Kirchner, and R. M. Dreizler, J. Phys. A **29**, 4423 (1996).
[18] A. Henne, H. J. Lüdde, and R. M. Dreizler, J. Phys. B **30**, L565 (1997).
[19] M. Keim, A. Werner, D. Hasselkamp, K.-H. Schartner, H. J. Lüdde, A. Achenbach, and T. Kirchner, J. Phys. B **38**, 4045 (2005).
[20] D. R. Schultz, M. R. Strayer, and J. C. Wells, Phys. Rev. Lett. **82**, 3976 (1999).
[21] X.-M. Tong, D. Kato, T. Watanabe, and S. Ohtani, Phys. Rev. A **62**, 052701 (2000).
[22] M. Chassid and M. Horbatsch, Phys. Rev. A **66**, 012714 (2002).
[23] R. Abrines and I. C. Percival, Proc. Phys. Soc. London **88**, 861 (1966).
[24] R. E. Olson and A. Salop, Phys. Rev. A **16**, 531 (1977).
[25] L. F. Errea, C. Illescas, L. Méndez, B. Pons, A. Riera, and J. Suárez, Phys. Rev. A **70**, 052713 (2004).
[26] P. S. Krstic, C. O. Reinhold, and D. R. Schultz, J. Phys. B **31**,

L155 (1998).
[27] C. Illescas, B. Pons, and A. Riera, Phys. Rev. A **63**, 062722 (2001).
[28] C. O. Reinhold and J. Burgdorfer, J. Phys. B **26**, 3101 (1993).
[29] A. L. Ford, J. F. Reading, and K. A. Hall, J. Phys. B **26**, 4537 (1993).
[30] F. Martín, J. Phys. B **32**, 501 (1999).
[31] B. Pons, Phys. Rev. Lett. **84**, 4569 (2000).
[32] B. Pons, Phys. Rev. A **63**, 012704 (2001); **64**, 019904(E) (2001).
[33] L. F. Errea, J. D. Gorfinkiel, C. Harel, H. Jouin, A. Macías, L. Méndez, B. Pons, and A. Riera, Phys. Scr., T **T62**, 27 (1996).
[34] R. K. Janev, Phys. Rev. A **53**, 219 (1996).
[35] E. A. Solov'ev, in *Proceedings of the XIX ICPEAC*, edited by L. J. Dubé em *et al.* (AIP Press, New York, 1995).
[36] G. I. Ivanovski and E. A. Solov'ev, Sov. Phys. JETP **77**, 887 (1993).
[37] R. K. Janev and L. P. Presnyakov, J. Phys. B **13**, 4233 (1980).
[38] B. H. Bransden and M. R. C. McDowell, *Charge Exchange and the Theory of Ion-Atom Collisions* (Clarendon Press, Oxford, 1992).
[39] C. Illescas and A. Riera, Phys. Rev. Lett. **80**, 3029 (1998).
[40] L. F. Errea, L. Méndez, B. Pons, A. Riera, and I. Sevila, Phys. Rev. A **67**, 022716 (2003).
[41] E. Y. Sidky and C. D. Lin, Phys. Rev. A **65**, 012711 (2001).
[42] L. F. Errea, C. Harel, H. Jouin, L. Méndez, B. Pons, and A. Riera, J. Phys. B **31**, 3257 (1998).
[43] A. T. Le, C. D. Lin, L. F. Errea, L. Méndez, A. Riera, and B. Pons, Phys. Rev. A **69**, 062703 (2004).
[44] L. F. Errea, C. Harel, H. Jouin, J. M. Maidagan, L. Méndez, B. Pons, and A. Riera, Phys. Rev. A **46**, 5617 (1992).
[45] L. F. Errea, C. Harel, H. Jouin, L. Méndez, B. Pons, and A. Riera, J. Phys. B **27**, 3603 (1994).
[46] C. Harel, H. Jouin, B. Pons, L. F. Errea, L. Méndez, and A. Riera, Phys. Rev. A **55**, 287 (1997).
[47] L. F. Errea, C. Harel, H. Jouin, L. Méndez, B. Pons, A. Riera, and I. Sevila, Phys. Rev. A **65**, 022711 (2002).
[48] A. R. Edmonds, *Angular Momentum in Quantum Mechanics* (Princeton University Press, Princeton, NJ, 1974).
[49] N. Stolterfoht, R. D. Dubois, and R. D. Rivarola, *Electron Emission in Heavy Ion-Atom Collisions* (Springer-Verlag, Berlin, 1997).
[50] R. Shakeshaft, Phys. Rev. A **18**, 1930 (1978).
[51] T. G. Winter, Phys. Rev. A **33**, 3842 (1986).
[52] I. Sevila, Ph.D. thesis, Universidad Autónoma de Madrid, Madrid (2003).
[53] M. B. Shah and H. B. Gilbody, J. Phys. B **14**, 2361 (1981).
[54] M. B. Shah, D. S. Elliot, and H. B. Gilbody, J. Phys. B **20**, 2481 (1987).
[55] M. B. Shah, J. Geddes, M. M. McLaughlin, and H. B. Gilbody, J. Phys. B **31**, L757 (1998).
[56] G. W. Kerby III, M. W. Gealy, Y.-Y. Hsu, M. E. Rudd, D. R. Schultz, and C. O. Reinhold, Phys. Rev. A **51**, 2256 (1995).
[57] D. S. F. Crothers and J. F. McCann, J. Phys. B **16**, 3229 (1983).
[58] G. M. McClure, Phys. Rev. **148**, 47 (1966).
[59] J. T. Park, J. E. Aldag, J. M. George, and J. L. Peacher, Phys. Rev. A **14**, 608 (1976).
[60] C. O. Reinhold, R. E. Olson, and W. Fritsch, Phys. Rev. A **41**, 4837 (1990).
[61] D. R. Bates and G. Griffing, Proc. Phys. Soc. London **66**, 64 (1953).
[62] C. R. Mandal, M. Mandal, and S. C. Mukherjee, Phys. Rev. A **42**, 1787 (1990).
[63] M. B. Shah, D. S. Elliot, P. McCallion, and H. B. Gilbody, J. Phys. B **21**, 2455 (1988).
[64] M. B. Shah and H. B. Gilbody, J. Phys. B **11**, 121 (1978).
[65] C. Illescas and B. Pons (unpublished).
[66] M. P. Hughes, J. Geddes, and H. B. Gilbody, J. Phys. B **27**, 1143 (1994).
[67] W. Fritsch, R. Shingal, and C. D. Lin, Phys. Rev. A **44**, 5686 (1991).
[68] M. B. Shah and H. B. Gilbody, J. Phys. B **15**, 413 (1982).
[69] M. B. Shah, T. V. Goffe, and H. B. Gilbody, J. Phys. B **11**, L233 (1978).
[70] J. Suárez, Ph.D. thesis, Universidad Autónoma de Madrid and Université de Bordeaux–I, Madrid (2005).
[71] A. Igarashi and T. Shirai, Phys. Rev. A **50**, 4945 (1994).
[72] T. V. Goffe, M. B. Shah, and H. B. Gilbody, J. Phys. B **12**, 3763 (1979).
[73] M. B. Shah and H. B. Gilbody, J. Phys. B **16**, 4395 (1983).
[74] J. R. Oppenheimer, Phys. Rev. **31**, 349 (1928).
[75] E. A. Solov'ev, J. Phys. B **38**, R153 (2005).
[76] H. A. Bethe and E. E. Salpeter, *Quantum Mechanics of One- and Two-electron Atoms* (Springer-Verlag, Berlin, 1957).
[77] D. Detleffsen, M. Anton, A. Werner, and K.-H. Schartner, J. Phys. B **27**, 4195 (1994).
[78] M. Anton, D. Detleffsen, and K.-H. Schartner, Nucl. Fusion Suppl. **3**, 51 (1992).
[79] M. Anton, D. Detleffsen, K.-H. Schartner, and A. Werner, J. Phys. B **26**, 2005 (1993).
[80] P. D. Fainstein, V. H. Ponce, and R. D. Rivarola, J. Phys. B **24**, 3091 (1991).